
Properties of Molecular Gas in Galaxies in Early and Mid Stages of Interaction. III. Resolved Kennicutt–Schmidt Law

Hiroyuki KANEKO,^{1,2} Nario KUNO,^{3,4} Daisuke IONO,^{2,5} Yoichi TAMURA,⁶
Tomoka TOSAKI,⁷ Kouichiro NAKANISHI,^{2,5} and Tsuyoshi SAWADA^{2,8}

¹Graduate School of Education, Joetsu University of Education, 1 Yamayashiki-machi, Joetsu, Niigata, 943-8512, Japan

²National Astronomical Observatory of Japan, 2-21-1 Osawa, Mitaka, Tokyo, 181-8588, Japan

³Graduate School of Pure and Applied Sciences, University of Tsukuba, 1-1-1 Tennodai, Tsukuba, Ibaraki, 305-8577, Japan

⁴Tomonaga Center for the History of the Universe, University of Tsukuba, Tsukuba, Ibaraki 305-8571, Japan

⁵Department of Astronomical Science, The Graduate University for Advanced Studies, 2-21-1 Osawa, Mitaka, Tokyo, 181-8588, Japan

⁶Division of Particle and Astrophysical Science, Graduate School of Science, Nagoya University, Furo-cho, Chikusa-ku, Nagoya, Aichi, 464-8602, Japan

⁷Department of Geoscience, Joetsu University of Education, 1, Yamayashiki-machi, Joetsu, Niigata, 943-8512, Japan

¹Graduate School of Pure and Applied Sciences, University of Tsukuba, 1-1-1 Tennodai, Tsukuba, Ibaraki, 305-8577, Japan

⁸Joint ALMA Observatory, Alonso de Cordova 3107, Vitacura, Santiago, Chile

*E-mail: hkaneko@juen.ac.jp

Received ; Accepted

Abstract

We study properties of the interstellar medium, an ingredient of stars, and star formation activ-

ity, in four nearby galaxy pairs in the early and mid stages of interaction for both a galaxy scale and a kpc scale. The galaxy-scale Kennicutt–Schmidt law shows that seven of eight interacting galaxies have a star formation rate within a factor of three compared with the best-fit of the isolated galaxies, although we have shown that molecular hydrogen gas is efficiently produced from atomic hydrogen during the interaction in the previous paper. The galaxy-scale specific star formation rate (sSFR) and star formation efficiency (SFE) in interacting galaxies are comparable to those in isolated galaxies. We also investigate SFE and the Kennicutt–Schmidt law on a kpc scale. The spatial distributions of SFE reveal that SFE is locally enhanced, and the enhanced regions take place asymmetrically or at off-centre regions. The local enhancement of SFE could be induced by shock. We find that the index of the Kennicutt–Schmidt law for the interacting galaxies in the early stage is 1.30 ± 0.04 , which is consistent with that of the isolated galaxies. Since CO emission, which is used in the Kennicutt–Schmidt law, is a tracer of the amount of molecular gas, this fact suggests that dense gas, which is more directly connected to star formation, is not changed at the early stage of interaction.

Key words: galaxies: individual (Arp 84, VV 219, VV 254, the Antennae Galaxies) — galaxies: interactions — galaxies: ISM — ISM: molecules

1 Introduction

Galaxy-galaxy interactions are one of the fundamental phenomena for galaxy evolution, as proved by the increase of merger rate along with the red-shift (e.g., Bridge, Carlberg, & Sullivan 2010). They significantly alter the morphological, dynamical, and chemical features of progenitors. Compared with isolated spiral galaxies, galaxies under close interaction with other galaxies tend to have higher star formation activity traced by $H\alpha$ (Bushouse 1987), radio continuum (Stoche 1978), and infrared (IR: Bushouse, Lamb, & Werner 1988) emission. What makes these drastic changes is an important issue for understanding the effects of the galaxy-galaxy interaction.

In this context, the properties of molecular gas are key to understanding the star formation in galaxies because cold molecular clouds fuel current and future star formation. Most of (ultra-)luminous infrared galaxies (U/LIRGs, whose IR luminosities of $L_{\text{IR}} > 10^{12}L_{\odot}$ and $> 10^{11}L_{\odot}$, respectively) found in the local Universe are interacting galaxies (Sanders et al. 1988). Therefore, a cause of active star formation in interacting galaxies have been examined

with the relationship between star formation rate (SFR) and molecular gas for U/LIRGs. Young et al. (1996), one of the pioneering works for this realm, exhibited that interacting galaxies have higher star formation efficiency (SFE: a ratio of SFR and molecular gas mass) than isolated galaxies. Violino et al. (2018) also statistically confirmed that close interacting galaxies have shorter depletion time (an inverse of SFE). From observations of nearby LIRGs with dense molecular gas tracers such as high- J CO, HCN, and HCO⁺ lines, it is suggested that a higher fraction of dense gas in interacting galaxies is likely to be the cause of their high SFE (Gao & Solomon 2004; Liu et al. 2015; Michiyama et al. 2016).

Another key investigation for the relationship between SFR and cold interstellar gas is the Kennicutt–Schmidt law (Schmidt 1959; Kennicutt 1998a). Observational studies on a galaxy scale have shown that the surface density of SFR and that of the interstellar medium (ISM) obey a power-law relation:

$$\log \Sigma_{\text{SFR}} = A + N \log \Sigma_{\text{ISM}}. \quad (1)$$

Observational studies of nearby isolated galaxies show N of 1.2–1.4 in both a galaxy and a kpc scale. Daddi et al. (2010) derived the Kennicutt–Schmidt law for local and high- z galaxies. They found that starburst galaxies like U/LIRGs form stars rapidly, while spiral galaxies and BzK galaxies show a long-lasting star formation. This result implies the physical mechanism of star formation in interacting galaxies is different from isolated spiral galaxies.

However, in most cases, these observational studies discussed only the galaxy-scale physical conditions due to the limitation of spatial resolution. Although there are observations that can resolve galactic structures, most of them focused on the interacting galaxies that already show active star formation. This bias hinders pursuing where and when star formation is enhanced during the interaction. Many numerical simulations have illustrated that molecular gas inflow is induced by galaxy-galaxy interactions (Barnes & Hernquist 1996; Teyssier, Chapon & Bournaud 2010; Hopkins et al. 2013). The inflow makes the density of molecular gas high at the central region of galaxies, and then such molecular gas efficiently converts into stars. Observational studies reported that the inflow occurs in some interacting galaxies (e.g., Iono, Yun & Mihos 2004). However, not all the interacting galaxies with active star formation show the central starburst. For example, the most active star-forming site of the Antennae Galaxies, one of the representative interacting galaxies in the local Universe, are not at their centres but their overlap region (Whitmore et al. 1999). For understanding the effect of a galaxy-interaction event on an enhancement of star formation, three aspects should be important: (1) before or at the onset of the enhancement of star formation (i.e., not being a merging phase), (2) molecular

gas as an ingredient for star formation, and (3) resolving galactic structures.

Following the strategies listed above, Kaneko et al. (2013) (Paper I) observed four interacting galaxies in the early and mid stages of the interaction in $^{12}\text{CO}(J = 1-0)$ (hereafter, we denote CO) emission line. Since they mapped in kpc scale, which can resolve galactic structures, it is suitable for investigations of properties of the ISM under the effect of the interaction. Using Paper I data, Kaneko et al. (2017) (hereafter Paper II) illustrated that a galaxy-scale molecular gas fraction in interacting galaxies is higher than isolated galaxies, even in the early stage of the interaction. Furthermore, they showed that high molecular gas fraction is due to an efficient conversion from atomic gas to molecular gas by external pressure using theoretical model fitting. Since molecular gas is fuel for stars, these results imply that star formation activity in these interacting galaxies is also affected by the interactions.

In this paper, we focus on relationships between gas contents and star formation activity. The structure of this paper is as follows: We explain the data we used, including isolated spiral galaxies for comparison in section 2. Section 3 presents derived values and describe the derivation of the dust-extinction corrected star formation rate. We discuss star formation activity such as specific star formation rate, star formation efficiency, and the Kennicutt–Schmidt law on a galaxy scale in section 4. Then we discuss the kpc-scale SFR and SFE in section 5. The spatially-resolved Kennicutt–Schmidt law is discussed in section 6. Finally, we summarise this study in section 7.

2 Data

We collect data covering an entire system of interacting galaxies in order to understand a relationship between ISM contents and star formation properties in interacting galaxies. We set a condition on the sample to resolve galactic structures (a linear resolution of < 10 kpc). We select sample galaxy pairs that are in the early and the mid stages of the interaction. The stage definition is based on Zhu, Seaquist & Kuno (2003). The early stage of the interaction is defined by the separation of nuclei and morphology. The interacting galaxies in the early stage fulfil $R < 1.5D_{25}$, where R is the projected separation between the nuclei, and D_{25} is the diameter of the primary galaxy, using the brightness contour, $B_T = 25$ mag arcsec $^{-2}$. In addition, they also show small morphological disturbances. Therefore, we classify galaxies contacting the celestial sphere and having a severely disturbed morphology, i.e., colliding galaxies, as the mid stage of interaction. We obtain data of molecular gas (CO), atomic hydrogen gas (HI), old stars (K_s -band), and star formation tracers ($H\alpha$, FUV, $8 \mu\text{m}$ and $24 \mu\text{m}$). We also use a dataset of

CO, HI, K_s -band, H α , FUV, 8 μm , and 24 μm images of isolated spiral galaxies for comparison.

2.1 CO data

We used CO data for interacting galaxies from Paper I. The dataset was obtained with the Nobeyama 45-m radio telescope whose effective angular resolution is $19''.3$ and pixel size is $7''.5$. An interacting galaxy sample consists of four systems: Arp 84, VV 219, VV 254, and the Antennae Galaxies. The sensitivities of the data are 3×10^{-3} – 1×10^{-2} Jy km s $^{-1}$ arcsec $^{-2}$. Based on our definition, Arp 84, VV 219, and VV 254 are the early stage of interaction, while the Antennae Galaxies are in the mid stage. The similar recession velocities of these galaxy pairs suggest they are clearly colliding systems as opposed to apparent close pairs due to projection effects. Figure 1 shows K_s -band images with the CO contours of interacting galaxies. Details of the CO data are summarised in table 1.

We used the CO data for isolated spiral galaxies from Nobeyama CO Atlas (Kuno et al. 2007) for comparison. Since the CO dataset of this atlas was obtained with the Nobeyama 45-m radio telescope as our interacting galaxy sample, it is a suitable CO dataset for comparison purposes. We only used galaxies that all other tracers are available. To remove other environmental effects, we excluded the galaxies belonging to the Virgo and Coma clusters. As a result, 11 of 40 galaxies were used for analysis (see table 2).

Both datasets are obtained with the on-the-fly (OTF) method, resulting in almost constant noise throughout the map. The typical systematic error of intensity calibration for the Nobeyama 45-m telescope is about 15%. The data with the pointing error worse than $5''$, which is higher than the grid spacing of $7''.5$, are removed in the data reduction.

2.2 HI data

All HI data for interacting galaxies were acquired with the Very Large Array (VLA)¹. The HI images for Arp 84, VV 219, VV 254, and the Antennae Galaxies were taken from the VLA archive, Condon et al. (1993), Iono, Yun & Ho (2005), and Hibbard et al. (2001), respectively. Since the VLA is an interferometer, the calibration error is nearly constant throughout a map. The angular resolutions of the HI data are typically $10''$ – $15''$, and all of them are higher than CO data.

¹ The National Radio Astronomy Observatory is a facility of the National Science Foundation operated under cooperative agreement by Associated Universities, Inc.

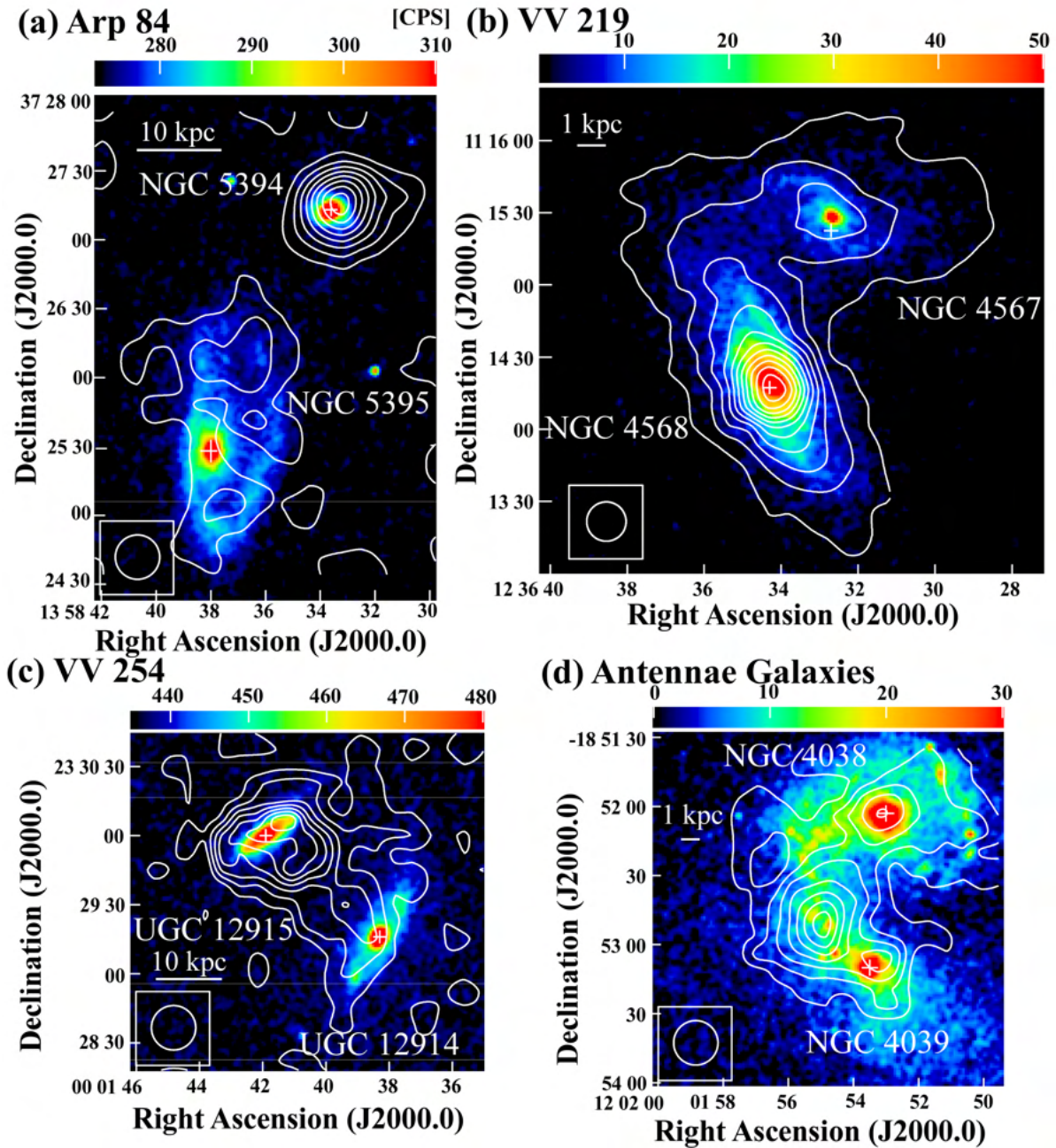


Fig. 1. 2MASS K_s -band image with CO integrated intensity contours for interacting galaxies. Circles in the bottom-left corner of each panel are the beam size of CO ($19''.3$). (a) Arp 84 image. The CO contour levels are $2.81 \times 2, 3, 4, \dots$ K km s $^{-1}$. The crosses represent the galactic centres of NGC 5394 (top right) and NGC 5395 (bottom left). (b) The same as (a) but for VV 219. The contours are $7.20 \times 1, 2, 3, \dots$ K km s $^{-1}$. The crosses represent the galactic centres of NGC 4567 (top right) and NGC 4568 (bottom left). (c) The same as (a) but for VV 254. The contours are $6.63 \times 1, 2, 3, 4, \dots$ K km s $^{-1}$. The crosses represent the galactic centres of UGC 12914 (bottom right) and UGC 12915 (top left). (d) The same as (a) but for the Antennae Galaxies. The contours are $23.7 \times 1, 2, 3, \dots$ K km s $^{-1}$. The crosses represent the galactic centres of NGC 4038 (top) and NGC 4039 (bottom).

Table 1. Interacting galaxies.

Pair Name	Galaxy	Morphology	Distance (Mpc)	Inclination (deg)	Orbit	R_{K20} (arcsec)	Resolution (kpc)
(1)	(2)	(3)	(4)	(5)	(6)	(7)	(8)
Arp 84	NGC 5394	SB(s)b pec	53	0	P	34	5.0
	NGC 5395	SA(s)b pec		58	R	71	
VV 219	NGC 4567	SA(rs)bc	16	44	R	70	1.5
	NGC 4568	SA(rs)bc		58	R	94	
VV 254	UGC 12914	(R)S(r)cd pec	62	61	H	55	5.8
	UGC 12915	S?		73	H	40	
Antennae Galaxies	NGC 4038	SB(s)m pec	21	—	P	73	2.0
	NGC 4039	SA(s)m pec		—	P	81	

Note — Column (1): Pair name. Column (2): Name of the constituent galaxy. Column (3): Morphological type from NED. Column (4): Distance to the pair. Column (5): Inclination angle. Reference: Kaufman et al. (1999) for Arp 84, this work for VV 219 and Giovanelli et al. (1986) for VV 254. Since the Antennae Galaxies have complex morphologies, the inclination is not fixed. Column (6): Orbital type judging from their morphology; P, R, H represent a prograde, retrograde and head-on collision, respectively. Column (7): The fitted radius at 20 mag arcsec⁻² in the K_s -band in Paper I. Column (8): Linear spatial resolution corresponding to the effective angular resolution of CO, 19.''3, at the distance of galaxy pairs.

Table 2. Control isolated galaxies.

Name	Morphology	Velocity (km s ⁻¹)	Distance (Mpc)	Inclination (deg)	R_{K20} (arcsec)
(1)	(2)	(3)	(4)	(5)	(6)
NGC 253	SAB(s)c	227	2.5	75	630.2
NGC 2903	SAB(rs)bc	549	6.3	67	163.0
NGC 3184	SAB(rs)cd	594	8.7	21	114.6
NGC 3351	SB(r)b	778	10.1	40	116.3
NGC 3521	SAB(rs)bc	792	7.2	63	164.4
NGC 3627	SAB(s)b	715	11.1	52	185.0
NGC 4736	(R)SA(r)ab	317	4.3	40	172.3
NGC 5055	SA(rs)bc	503	7.2	61	204.2
NGC 5236	SAB(s)c	514	4.5	24	312.4
NGC 5457	SAB(rs)cd	255	7.2	18	236.3
NGC 6946	SAB(rs)cd	60	5.5	40	252.5

Note — Column (1): Galaxy name. Column (2): Morphological type. Column (3): Velocity in local standard of rest (Kuno et al. 2007). Column (4): Distance. Column (5): Inclination angle. Column (6): Radius at 20 magnitude arcsec⁻² in the K_s -band.

For isolated galaxies, we used the HI data obtained with the VLA by THINGS² except for NGC 253, whose data was taken with the Australia Telescope Compact Array (Boomsma et al. 2005). The THINGS datasets have two weighting images: natural weighting and robust weighting. We used the natural weighting, which leads to higher sensitivity with lower angular resolution. Each THINGS HI data of isolated galaxies has an angular resolution of about $10''$ – $15''$ with a grid spacing of $1''.5$. The main uncertainty for HI data is flux calibration error ($\sim 5\%$) and continuum subtraction (depending on the data, but low-quality data is not in public: Walter et al. 2008). Since the HI data of NGC 253 has an angular resolution of $70''$, which is much larger than other samples, we only use this data to discuss the galaxy scale.

2.3 K_s data

In order to derive stellar mass, we used the K_s -band images. All data were taken from the Two Micron All Sky Survey (2MASS) catalogue³ (Skrutskie et al. 2006; Jarrett et al. 2003). The point spread function (PSF) for K_s is about $2''$ – $3''$. Photometric zero-point calibration is accurate to 2-3%, and the relative intensity calibration error of 2MASS data is uniformly 2-3% over the sky.

2.4 $H\alpha$ and FUV data

We collected $H\alpha$ data from published papers (Koopmann, Kenney & Young 2001; Xu et al. 2000). The typical systematic flux calibration errors, including continuum subtraction and calibration errors, are estimated to be 20-30% in total $H\alpha$ fluxes. Since Arp 84 has no available $H\alpha$ image, we used the Galaxy Evolution Explorer (GALEX) FUV images retrieved from MultiMission Archive at Space Telescope Science Institute (MAST). The original observations were a part of the GALEX Nearby Galaxies Survey (NGS) (Gil de Paz et al. 2007).

For isolated galaxies, $H\alpha$ images are obtained from Kennicutt et al. (2008) except for NGC 3184, which was observed by Young et al. (1996). The data reduction processes are similar to Koopmann, Kenney & Young (2001).

The PSFs of $H\alpha$ and FUV for interacting galaxies and isolated galaxies are typically $2''$ and $4''$ – $4''.5$, respectively. These are much smaller than the angular resolution of CO and HI data.

² This work made use of THINGS, ‘The HI Nearby Galaxy Survey’ (Walter et al. 2008)

³ This publication makes use of data products from the Two Micron All Sky Survey, which is a joint project of the University of Massachusetts and the Infrared Processing and Analysis Center/California Institute of Technology, funded by the National Aeronautics and Space Administration and the National Science Foundation

2.5 MIPS 24 μm and IRAC 8 μm data

Star formation activity estimated from only $\text{H}\alpha$ or FUV is underestimated due to dust absorption. For correcting the dust absorption, we used the 24 μm Multiband Imaging Photometer (MIPS: Rieke et al. 2004) and 8 μm Infrared Array Camera (IRAC: Fazio et al. 2004) datasets of the basic calibrated data (BCD) created by the Spitzer Science Center (SSC) pipeline from the Spitzer Space Telescope (Werner et al. 2004) data archive⁴. For IRAC 8 μm and MIPS 24 μm datasets, thermal noise and calibration uncertainty are typically less than 10% (also see Smith et al. 2007). The PSFs of IRAC 8 μm and MIPS 24 μm for all samples are about 2'' and 5'', respectively.

3 Derived properties of molecular gas, atomic gas, stars, and star formation activity

We derive molecular hydrogen, atomic hydrogen, stellar mass, and SFR from collected data. Molecular hydrogen gas mass is derived from CO data, assuming the Galactic $I_{\text{CO}} - N_{\text{H}_2}$ conversion factor of $1.8 \times 10^{20} [\text{cm}^{-2} (\text{K km s}^{-1})^{-1}]$ (Dame et al. 2001). The uncertainties in the integrated intensity were estimated to be less than 15% for each map due to the rms error in the spectrum and the error in the determination of the baseline (the details are described in Paper I).

Since the conversion factor varies from one galaxy to another and within each galaxy (Sandstrom et al. 2013), the scatter and the uncertainty of the Kennicutt–Schmidt relation become larger when a unique conversion factor is used. From both observational and theoretical approaches, the conversion factor gets lower in high surface density environments such as ULIRGs (Bolatto, Wolfire & Leroy 2013). Although our sample interacting galaxies are not CO-bright compared with ULIRGs, some targets are known to have lower conversion factors (Zhu, Seaquist & Kuno 2003; Zhu et al. 2007). If we suppose that the conversion factor in all our sample interacting galaxies is lower than the Galactic conversion factor, then the measurements of the surface density of molecular gas and total gas are overestimated. The lower conversion factor makes SFE and the slope of the Kennicutt–Schmidt law higher than the values we will investigate.

We do not take into account the errors, including the observational uncertainties and the variation of the $I_{\text{CO}} - N_{\text{H}_2}$ conversion factor in deriving the index and coefficient of the Kennicutt–Schmidt law. In spiral galaxies, the standard deviation of the $I_{\text{CO}} - N_{\text{H}_2}$ conversion

⁴ This work is based on observations made with the Spitzer Space Telescope, which is operated by the Jet Propulsion Laboratory, California Institute of Technology under a contract with NASA.

Table 3. Basic properties of interacting galaxies.

Galaxy	M_{H_2} ($10^9 M_\odot$)	M_{HI} ($10^9 M_\odot$)	M_* ($10^9 M_\odot$)	$L_{\text{H}\alpha}(L_{\text{FUV}})$ ($10^{40(42)} \text{ erg s}^{-1}$)	$L_{24\mu\text{m}}(L_{8\mu\text{m}})$ ($10^{42} \text{ erg s}^{-1}$)	Reference [†]
(1)	(2)	(3)	(4)	(5)	(6)	(7)
NGC 5394	4.8	0.08	7.9	7.4 (5.1)	2.9	1, 3, 6
NGC 5395	8.0	5.7	26.7	1.3 (3.1)	10.7	1, 3, 6
NGC 4567	1.3	0.2	1.7	3.8	0.8	1, 4, 6
NGC 4568	3.0	1.1	5.2	7.9	2.0	1, 4, 6
UGC 12914	10.3	6.2	20.5	5.1	8.3	1, 3, 7
UGC 12915	14.9	5.1	11.6	3.1	4.9	1, 3, 7
NGC 4038	6.2	2.5	8.2	47.2	2.7	2, 5, 7
NGC 4039	3.2	1.0	7.2	50.8	2.1	2, 5, 7

Note — Column (1): Galaxy name. Column (2): Mass of molecular hydrogen. Column (3): Mass of atomic hydrogen. Column (4): Stellar mass. Column (5): $\text{H}\alpha$ luminosity. For Arp 84 and VV 254, FUV luminosity. Column (6): $24 \mu\text{m}$ luminosity. For Arp 84, $8 \mu\text{m}$ luminosity. $L_{24\mu\text{m}}$ and $L_{8\mu\text{m}}$ are monochromatic luminosity, νL_ν . For the 8.0 and $24 \mu\text{m}$ bands, the effective frequencies used were 8.45×10^{13} and 1.27×10^{13} Hz. Column (7): References of the HI, $\text{H}\alpha$, FUV, $24 \mu\text{m}$, and $8 \mu\text{m}$ data.

References: 1.Iono, Yun & Ho (2005); 2.Hibbard et al. (2001); 3. GALEX NGS (Gil de Paz et al. 2007);

4.Koopmann, Kenney & Young (2001); 5.Xu et al. (2000); 6. Smith et al. (2007); 7. Spitzer archive.

factor is 0.3 dex (Sandstrom et al. 2013). So, if this variation also suits to interacting galaxies, we expect the surface density of molecular gas has an uncertainty factor of at least 0.4 dex.

Mass of atomic hydrogen gas is calculated from HI assuming an optically thin emission, $M_{\text{HI}}[M_\odot] = 2.36 \times 10^5 D^2 S_{\text{HI}}$, where D is the distance in megaparsec, and S_{HI} is the integrated flux of HI in Jy km s^{-1} . Stellar mass is derived from K_s -band luminosity using a mass-to-light ratio of 0.95 (M_*/L_{K_s}) [M_\odot/L_\odot] (Bell et al. 2003). The derived fundamental quantities from the collected data for interacting galaxies and isolated galaxies are summarised in tables 3 and 4, respectively.

We derived dust-extinction corrected SFR. We used three calibration methods to correct the dust extinction; that is, we calculated SFR using $\text{H}\alpha$ (or FUV for Arp 84 and VV 254) and MIPS $24 \mu\text{m}$ (or IRAC $8 \mu\text{m}$ for Arp 84) data. Based on the method proposed by Calzetti et al. (2007), the extinction of $\text{H}\alpha$ by surrounding dust is corrected using Spitzer MIPS $24 \mu\text{m}$ data. We also used similar methods for FUV emission using Spitzer MIPS $24 \mu\text{m}$ or IRAC $8 \mu\text{m}$ data (Zhu et al. 2008). The calibration equations are as follows:

$$L_{\text{H}\alpha(\text{corr})} = L_{\text{H}\alpha(\text{obs})} + (0.032 \pm 0.006)L_{24\mu\text{m}} \quad (2)$$

$$L_{\text{FUV}(\text{corr})} = L_{\text{FUV}(\text{obs})} + 6.31L_{24\mu\text{m}} \quad (3)$$

$$= L_{\text{FUV}(\text{obs})} + 3.02L_{8\mu\text{m}}, \quad (4)$$

Table 4. Basic properties of isolated galaxies.

Galaxy	M_{H_2} ($10^9 M_\odot$)	$M_{\text{H I}}$ ($10^9 M_\odot$)	M_* ($10^9 M_\odot$)	$L_{\text{H}\alpha}$ (10^{40} erg s $^{-1}$)	$L_{24\mu\text{m}}$ (10^{42} erg s $^{-1}$)	Reference
(1)	(2)	(3)	(4)	(5)	(6)	(7)
NGC 253	1.6	1.0	4.7	3.9	13.7	1, 4, 7
NGC 2903	1.6	2.2	3.5	5.9	4.2	2, 4, 7
NGC 3184	1.1	1.9	1.5	6.9	1.6	2, 3, 5
NGC 3351	1.1	1.2	4.0	4.6	3.7	2, 4, 6
NGC 3521	2.9	3.6	5.4	8.1	4.1	2, 4, 5
NGC 3627	8.8	1.2	1.3	15.7	13.4	2, 4, 6
NGC 4736	0.4	0.3	4.0	2.4	1.5	2, 4, 5
NGC 5055	2.9	6.8	6.2	9.8	4.5	2, 4, 5
NGC 5236	2.0	1.7	6.2	18.3	12.0	2, 4, 7
NGC 5457	3.2	14.2	4.7	24.7	8.2	2, 4, 7
NGC 6946	4.0	3.6	5.9	25.1	9.1	2, 4, 5

Each column is described as the same manners as table 3.

References: 1. Boomsma et al. (2005); 2. Walter et al. (2008); 3. Young et al. (1996); 4. Kennicutt et al. (2008); 5. Smith et al. (2007); 6. Dale et al. (2005); 7. Dale et al. (2009)

where the luminosities are in erg s $^{-1}$, and L_{FUV} , $L_{24\mu\text{m}}$ and $L_{8\mu\text{m}}$ are monochromatic luminosity νL_ν . ν is the effective frequency and L_ν is the luminosity of the source at the image. Since Calzetti et al. (2007) report that the extinction correction using 24 μm is better than using 8 μm , we used 24 μm data except for Arp 84. For Arp 84, we used 8 μm data to calculate SFR because 24 μm emission is saturated in NGC 5394, one of the constituent galaxies of Arp 84.

After the extinction correction, SFR was calculated from H α using the equation Calzetti et al. (2007) proposed. To calculate SFR from FUV data, we adopt the equation introduced by Bruzual & Charlot (2003) instead of Kennicutt (1998b) because it is adjusted for the GALEX FUV data. These equations are as follows:

$$\text{SFR} [M_\odot \text{ yr}^{-1}] = 5.3 \times 10^{-42} L_{\text{H}\alpha(\text{corr})} [\text{erg s}^{-1}] \quad (5)$$

$$\text{SFR} [M_\odot \text{ yr}^{-1}] = 6.4 \times 10^{-41} L_{\text{FUV}(\text{corr})} [\text{erg s}^{-1}]. \quad (6)$$

In this paper, we do not include the systematic errors introduced by observations in the error estimation. As described in section 2, the systematic errors for each data range from a few to 30% due to flux calibration, continuum subtraction, or contamination of [N II] lines. Therefore, we expect the derived SFR to have an uncertainty factor of 0.4 dex, which is the same as the molecular gas mass estimate.

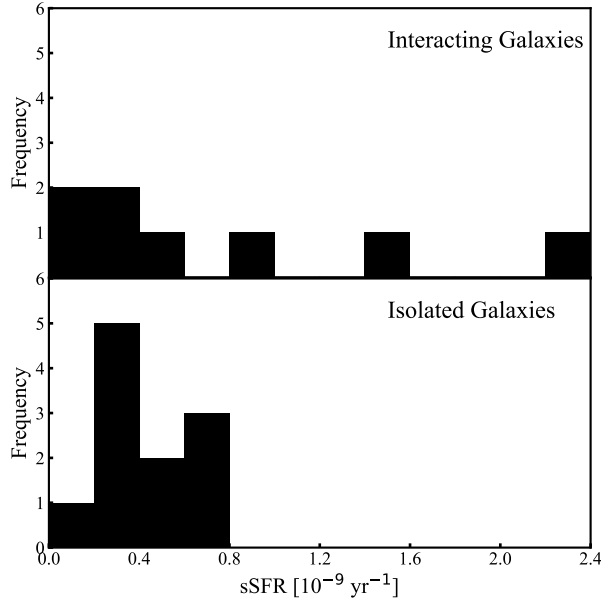


Fig. 2. Histograms of specific star formation rate for the interacting galaxies (upper panel) and the isolated galaxies (lower panel).

4 Galaxy-scale star formation activity

Previous works have discussed differences in the galaxy-scale star formation activities, ISM, and stellar contents between interacting galaxies and isolated galaxies (e.g., Young et al. 1996; Saintonge et al. 2011; Pan et al. 2018). In order to check whether our sample shows enhanced star formation activity on a galaxy scale, we compare galaxy-scale star formation activities with stellar and interstellar gas components.

First, we examine the specific star formation rate (sSFR), defined as SFR per stellar mass, SFR/M_* . The sSFR represents recent star formation activity. The histogram of sSFR is shown in figure 2. The dispersion of sSFR in interacting galaxies is larger than in isolated galaxies (tables 5 and 6). NGC 4038 and NGC 4039, both of which are a part of the Antennae Galaxies, have sSFR higher than $1.0 \times 10^{-9} \text{ yr}^{-1}$. Interacting galaxies have an average of sSFR of $(7.0 \pm 5.0) \times 10^{-10} \text{ yr}^{-1}$, while that of the isolated galaxies is $(4.1 \pm 2.0) \times 10^{-10} \text{ yr}^{-1}$. The median of sSFR is $4.0 \times 10^{-10} \text{ yr}^{-1}$ for interacting galaxies and $3.4 \times 10^{-10} \text{ yr}^{-1}$ for the isolated galaxies. The Kolmogorov–Smirnov test for sSFR shows that the current star formation activity of interacting galaxies in the early stage, on average, is as same as isolated galaxies (p -value of 0.42). The result is consistent with previous studies (Knapen, Cisternas, & Querejeta 2015; Pan et al. 2018) and implies interacting galaxies in the early stage do not show the burst of star formation as we expected that they are before or at the onset of the enhancement of star formation.

Although many studies suggest that molecular gas governs star formation, the contribu-

Table 5. Galaxy-scale star formation properties of interacting galaxies.

Galaxy	SFR ($M_{\odot} \text{ yr}^{-1}$)	sSFR (10^{-10} yr^{-1})	SFE _{mol} (10^{-10} yr^{-1})	SFE _{gas} (10^{-10} yr^{-1})
NGC 5394	4.9	8.0	10.2	10.0
NGC 5395	3.1	1.4	3.9	2.3
NGC 4567	0.67	4.3	5.2	4.5
NGC 4568	1.5	3.6	5.0	3.7
UGC 12914	1.6	1.0	1.6	1.0
UGC 12915	4.2	3.1	2.8	2.1
NGC 4038	8.4	14.8	13.5	9.7
NGC 4039	9.5	22.3	29.7	22.6

tion of atomic gas (HI) on star formation is still under debate. Bigiel et al. (2008) found that the surface density of HI gas saturates around $\Sigma_{\text{ISM}} \simeq 10 M_{\odot} \text{ pc}^{-2}$ and it is not connected to the star formation. Takeuchi et al. (private communication) reached the same conclusion using a larger dataset. However, recent studies suggest atomic hydrogen directly contributes to star formation activity (Fukui et al. 2019). Therefore, this paper will investigate the relationship between star formation and two ISM masses: molecular hydrogen gas and total hydrogen gas (a sum of HI and H₂ masses).

We derive two galaxy-scale SFEs, i.e., SFE_{mol} and SFE_{gas}, defined as the following equations:

$$\text{SFE}_{\text{mol}} [\text{yr}^{-1}] = \text{SFR}/M_{\text{H}_2}, \quad (7)$$

$$\text{SFE}_{\text{gas}} [\text{yr}^{-1}] = \text{SFR}/(M_{\text{H}_2} + M_{\text{HI}}). \quad (8)$$

While all isolated galaxies have lower SFE_{gas} than 10^{-9} yr^{-1} , two of eight interacting galaxies have SFE_{gas} higher than 10^{-9} yr^{-1} . However, the p -values of the Kolmogorov–Smirnov test for SFE_{mol} and SFE_{gas} are 0.42 and 0.52, respectively. These results indicate that both SFE_{mol} and SFE_{gas} for interacting galaxies and isolated galaxies are obtained from the same parents, consistent with Casasola, Bettoni & Galletta (2004). Young et al. (1996) reported that global SFE_{gas} in strongly interacting galaxies is higher than those found in normal spiral galaxies. The discrepancy might be caused by the increasing SFE as a function of the merger stage.

All derived properties for the interacting galaxies and the isolated galaxies are summarised in tables 5 and 6. Table 7 shows the mean galaxy-scale properties of interacting galaxies and the isolated galaxies.

A galaxy-scale relationship between the surface density of SFR and ISM contents, i.e.,

Table 6. Galaxy-scale star formation properties of the isolated galaxies.

Galaxy	SFR ($M_{\odot} \text{ yr}^{-1}$)	sSFR (10^{-10} yr^{-1})	SFE _{mol} (10^{-10} yr^{-1})	SFE _{gas} (10^{-10} yr^{-1})
NGC 253	2.5	6.3	15.6	9.6
NGC 2903	1.0	3.4	6.3	2.6
NGC 3184	0.6	5.6	5.5	2.0
NGC 3351	0.9	2.6	8.2	3.9
NGC 3521	1.1	2.4	3.8	1.7
NGC 3627	3.1	2.9	3.5	3.1
NGC 4736	0.4	1.1	10.0	5.7
NGC 5055	1.1	2.1	3.8	1.1
NGC 5236	3.3	6.4	16.5	8.9
NGC 5457	2.7	6.9	8.4	1.6
NGC 6946	2.9	5.8	7.3	3.8

Table 7. Mean star formation properties of interacting galaxies and isolated galaxies.

Quantities*	Interacting Galaxies	Isolated Galaxies
Number	8	11
M_{H_2} [$10^{10} M_{\odot}$]	8.0 ± 7.0	3.4 ± 2.9
SFR [$M_{\odot} \text{ yr}^{-1}$]	4.1 ± 3.3	1.5 ± 1.2
sSFR [10^{-10} yr^{-1}]	7.3 ± 7.0	4.1 ± 2.0
SFE _{mol} [10^{-10} yr^{-1}]	9.0 ± 8.7	8.1 ± 4.3
SFE _{gas} [10^{-10} yr^{-1}]	7.0 ± 6.7	4.0 ± 2.8

*The errors are the 1σ uncertainties.

the Kennicutt–Schmidt law using Σ_{mol} is shown in figure 3(top). The best-fitting power-law function for isolated galaxies is

$$\log \Sigma_{\text{SFR}} = -(8.98 \pm 0.17) + (0.86 \pm 0.13) \log \Sigma_{\text{mol}}, \quad (9)$$

where Σ_{SFR} and Σ_{mol} are the surface density of SFR [$M_{\odot} \text{ yr}^{-1} \text{ pc}^{-2}$] and H_2 mass [$M_{\odot} \text{ pc}^{-2}$], respectively. Σ_{SFR} and Σ_{mol} are derived assuming that all star-forming regions and molecular gas are within $R_{\text{K}20}$. Although the dynamic range is narrow and the number of galaxies is small, the best least-squares fit for the isolated galaxies is consistent with the results of a much larger sample from the COLD GASS survey, which shows the index of 0.86 ± 0.21 (Saintonge et al. 2012). We found no clear difference between interacting galaxies and isolated galaxies in the Kennicutt–Schmidt law: seven out of eight interacting galaxies have not enhanced SFRs by more than a factor of 3 compared to the best-fit line for the isolated galaxies.

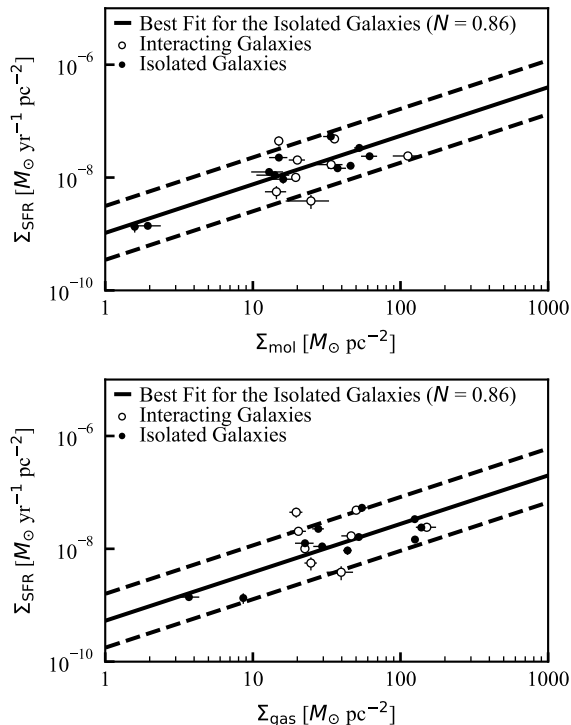


Fig. 3. Global Kennicutt–Schmidt law. (Top) Relationship between the surface density of star formation rate and molecular hydrogen gas mass for the interacting galaxies and the isolated galaxies. (Bottom) Relationship between the surface density of star formation rate and total gas mass for the interacting galaxies and the isolated galaxies. The line is the best least-squares fit for all isolated galaxies, and the dashed lines represent SFR is enhanced and decreased by a factor of three from the best fit.

Figure 3(bottom) shows the Kennicutt–Schmidt law adopting Σ_{gas} instead of Σ_{mol} . The best least-squares fit for isolated galaxies is

$$\log \Sigma_{\text{SFR}} = -(9.28 \pm 0.32) + (0.86 \pm 0.19) \log \Sigma_{\text{gas}}, \quad (10)$$

where Σ_{gas} is the surface density of total gas mass. The result is similar to the case of $\Sigma_{\text{SFR}} - \Sigma_{\text{mol}}$ relation: most interacting galaxies do not exceed the relation for isolated galaxies considering a scatter. The exceptional galaxy, NGC 4039, is the constituent galaxy of the Antennae Galaxies. The active star formation in the Antennae Galaxies is consistent with the previous studies that some interacting galaxies in the mid stage already show violent star formation (e.g., Zhu, Seaquist & Kuno 2003).

In the galaxy-scale Kennicutt–Schmidt law for both $\Sigma_{\text{SFR}} - \Sigma_{\text{mol}}$ and $\Sigma_{\text{SFR}} - \Sigma_{\text{gas}}$, star formation activity of our sample interacting galaxies have almost as same as that in isolated galaxies. Although several authors have reported a bi-modality in the Kennicutt–Schmidt law (sequences of starburst and discs) (Daddi et al. 2010; Genzel et al. 2010; Violino et al. 2018), our sample interacting galaxies do not show the bi-modality. The simulations performed by

Di Matteo et al. (2007) show that interacting galaxies are not in the sequence of starburst, while mergers have higher SFE than isolated galaxies. Our result is in agreement with their simulations.

5 Star formation rate and star formation efficiency on a kpc scale

To understand how star formation is enhanced during a galaxy interaction, it is important to reveal when and where properties of star formation are changed. As presented in section 4, our sample does not show enhanced star formation on a galaxy scale. However, it does not mean there is no local enhancement of star formation activity in these galaxy pairs. For this reason, we investigate kpc-scale star formation indicators (SFR, SFE_{mol} , and SFE_{gas}).

5.1 Maps of star formation rate and star formation efficiency

First, we calculate SFR using $H\alpha$ (or FUV for Arp 84 and VV 254) and MIPS 24 μm (or IRAC 8 μm for Arp 84) data in a map base. Since we will investigate not only SFR but also SFE_{mol} and SFE_{gas} , these data are convolved into the same angular resolution as CO data ($19''.3$), which is the lowest among the data and re-gridded to $7''.5$ per pixel. The reason for adopting a smaller pixel size than the Nyquist sampling rate ($\sim 10''$) is the limitation of the CO observations (the OTF method). In the OTF method, the antenna is driven continuously in a region to be mapped, and the data are acquired in a short interval. But antenna jitter and pointing accuracy do not make the data points align any regular grid. Thus, the data should be re-gridded onto a regular (rectangular) grid adopting a gridding convolution function during data reduction. This process makes the resultant beam size larger than the telescope beam (For the CO observations, whose rest frequency is 115.27 GHz, with the Nobeyama 45-m telescope, the telescope beam is $15''$) (see, figure 6 in Sawada et al. 2008). In addition, the peak temperature of a point source becomes lower. For example, if one choose the pixel size of $\sim 0.8 \times$ the original telescope beam, the data can be sampled with a Nyquist rate and the effective beam size becomes ~ 1.6 larger than the original telescope beam. However, such a large grid spacing leads to lower response to a point source ($0.4 \times$ the single-beam observation), which can not detect significant emission from some interacting galaxies. On the other hand, the smaller pixel size leads to the effective integration time is smaller, and thus the noise level becomes larger with the square of the pixel size. Considering these effects, we chose the pixel size of $7''.5$, which is the Nyquist sampling rate of the original telescope beam, in this paper. Note that this over-sampling leads to yield a better correlation in pixel-to-pixel comparison.

The effect of different sampling is discussed in Appendix.

On deriving SFR, we applied equations 5 and 6 on each pixel. We note that maps of SFR of interacting galaxies are not corrected for the inclination angle since the map contains two galaxies with a different inclination and is hard to handle. On the other hand, we correct the inclination angle effects when we plot the surface density of SFR in section 6.

To investigate where active star formation occurs, we also derive SFE_{mol} and SFE_{gas} maps for interacting galaxies based on equations 7 and 8. Note that maps of SFE_{mol} and SFE_{gas} are not affected by the inclination because the inclination angle affects Σ_{SFR} , Σ_{mol} and Σ_{gas} in the same manner. If SFR and gas masses have uncertainties of 0.4 dex, as noted in section 3, the uncertainties of SFE_{mol} and SFE_{gas} are roughly 55 and 60%, respectively.

Figures 4, 5, and 6 show maps of SFR, SFE_{mol} , and SFE_{gas} with contours of CO integrated intensity for interacting galaxies. Since the pointing accuracies of all observations are better than $5''$ as described in section 2, the spatial variations of each map are reliable. Therefore, we mask the values below 1σ noise error of the surface densities of SFR, molecular gas, and total gas in these maps.

Arp 84

Figure 4(a) shows that star formation activity in NGC 5394 (top-right) is high compared with NGC 5395 (bottom-left). FUV and $H\alpha$ (Roche et al. 2015) show weak star-forming regions along the spiral arm and a circular-shaped active star-forming region in the galactic centre. On the other hand, there is no star-forming region along the spiral arm in our SFR map. This could be due to low angular resolution. The peak of SFR, which is about $2.0 \times 10^{-8} M_{\odot} \text{yr}^{-1} \text{pc}^{-2}$, locates the centre of the galaxy, while the CO distribution is slightly lopsided toward the western side. With higher resolution CO data ($5.''5 \times 4.''3$), Iono, Yun & Ho (2005) also reported that the peak of CO is located westward from the centre of the galaxy. This discrepancy in the distribution between CO and SFR is emphasized in SFE maps in figures 5(a) and 6. The active star-forming region is slightly lopsided toward the nearer side to its companion, although the highest SFE is still at the centre of NGC 5394.

NGC 5395 shows the more complicated distribution of star-forming regions. The distribution of SFR differs from that of molecular gas (CO) and old stars (K_s) (see figure 1). A peak of SFR locates near the centre of NGC 5395 but $10''$ (2.5 kpc) to the north-east. Star-forming regions mainly trace the distribution of the old stars. The peak of SFR, which is found at the end of the tidal tail in CO, does not coincide with the peaks of CO.

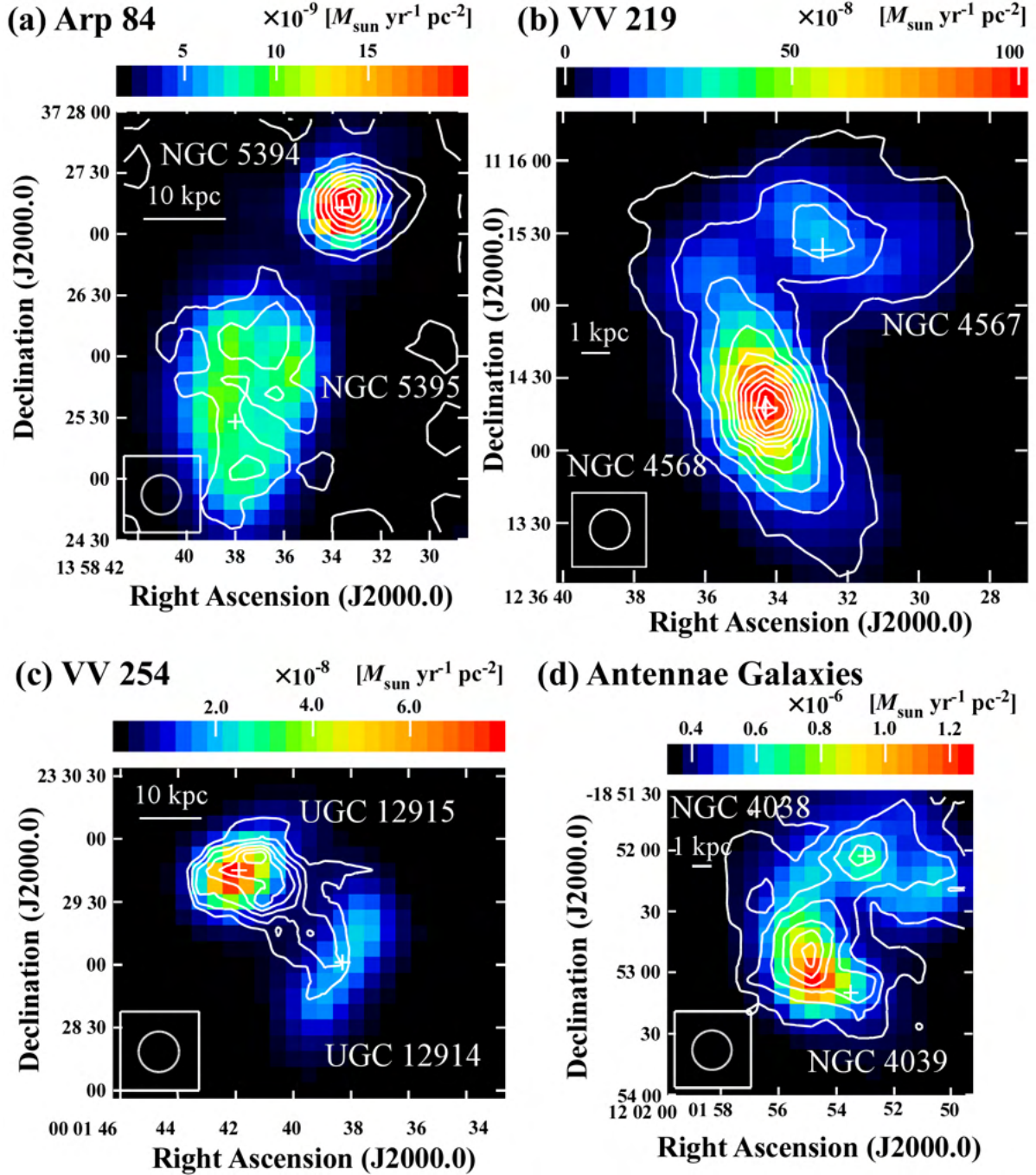


Fig. 4. (a) A SFR image with CO integrated intensity contours for Arp 84. The contours are $2.81 \times 2, 3, 4, \dots$ K km s⁻¹. (b) The same as (a) but for VV 219. The contours are $7.20 \times 1, 2, 3, \dots$ K km s⁻¹. (c) The same as (a) but for VV 254. The contours are $6.63 \times 2, 3, 4, \dots$ K km s⁻¹. (d) The same as (a) but for the Antennae Galaxies. The contours are $23.7 \times 1, 2, 3, \dots$ K km s⁻¹.

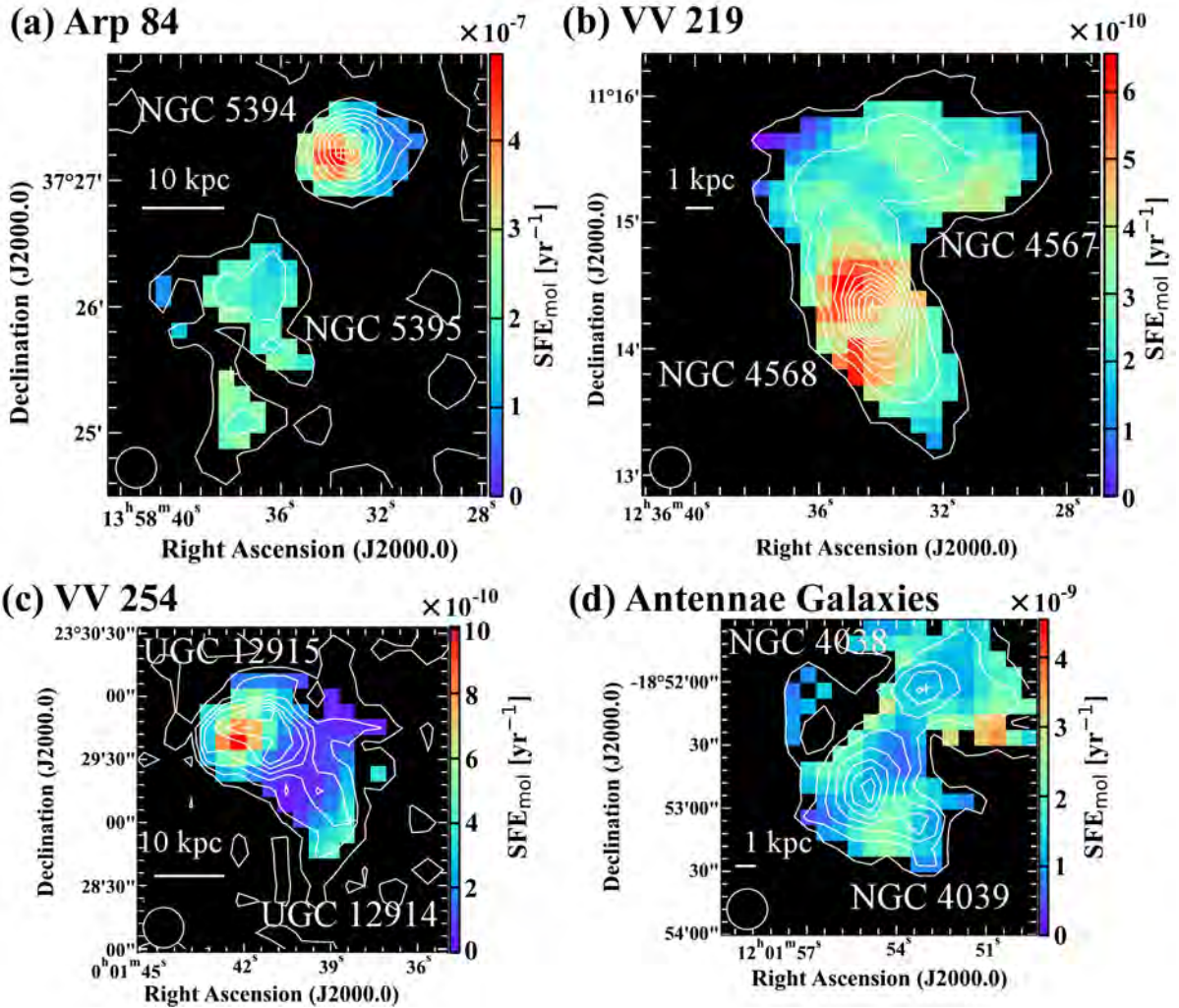


Fig. 5. (a) The same as figure 4(a) but a colour image is SFE_{mol} . (b) The same as figure 4(b) but a colour image is SFE_{mol} . (c) The same as figure 4(c) but a colour image is SFE_{mol} . (d) The same as figure 4(d) but a colour image is SFE_{mol} .

NGC 5395 has two local peaks in both SFE_{mol} and SFE_{gas} , which correspond to the peaks of SFR described above. The local peak of SFE_{mol} and SFE_{gas} at the tidal tail of NGC 5395 has comparable values to those at the centre of NGC 5395. The edge of the tidal tail, where CO gas is most abundant in NGC 5395, shows the lowest SFE_{mol} and SFE_{gas} in NGC 5395, even considering the uncertainty. This fact suggests active star formation with high SFEs cannot be caused only by the accumulation of molecular gas due to interaction.

VV 219

As illustrated in figure 4(b), the most intense star-forming activity in NGC 4568 (bottom-left) is at its centre, and SFR gradually decreases as the radius increases. These features are also

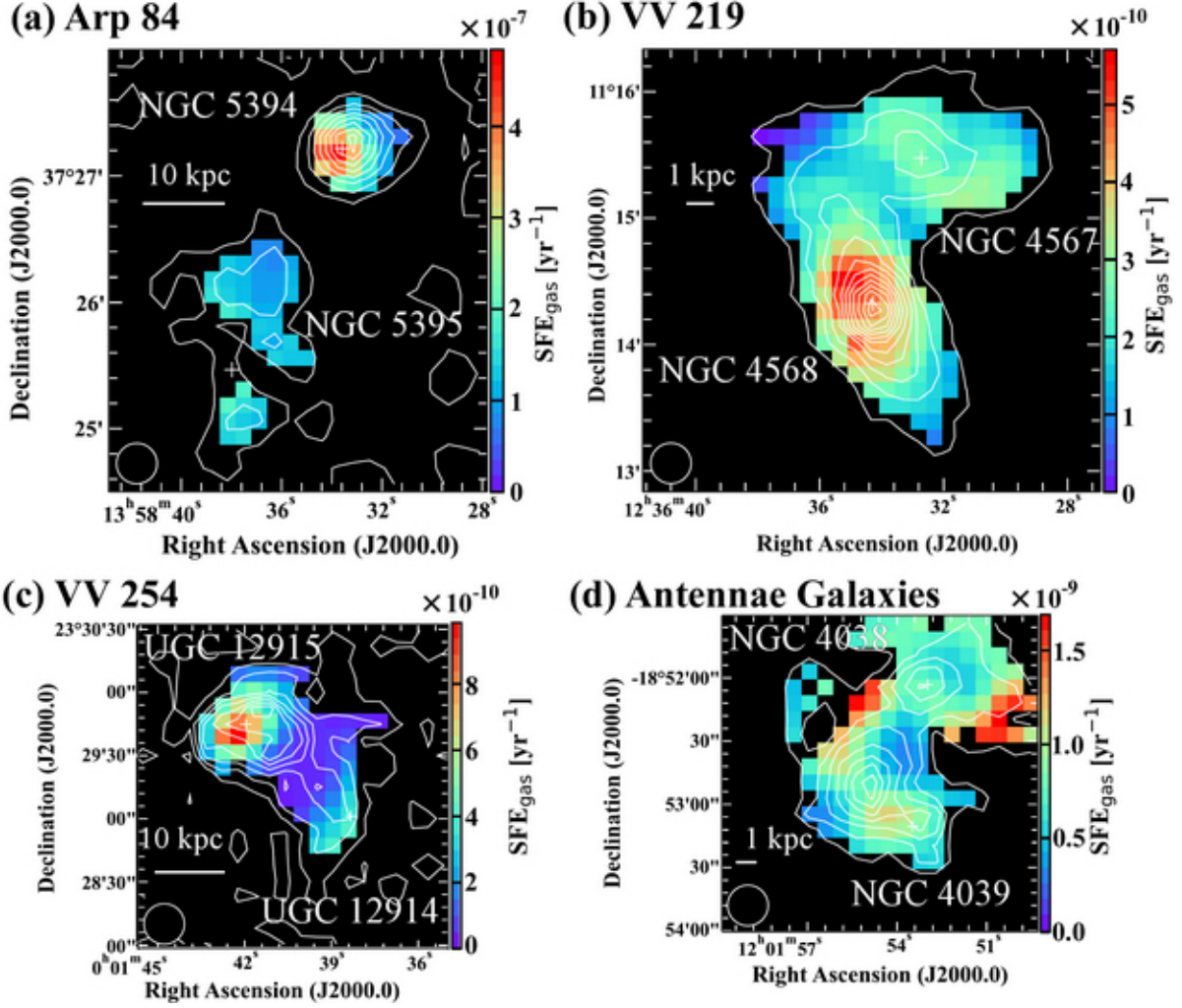


Fig. 6. (a) The same as figure 4(a) but a colour image is SFE_{gas} . (b) The same as figure 4(b) but a colour image is SFE_{gas} . (c) The same as figure 4(c) but a colour image is SFE_{gas} . (d) The same as figure 4(d) but a colour image is SFE_{gas} .

seen in isolated spiral galaxies. The active star formation of NGC 4567 (top-right) takes place along its spiral arms. The overlap region shows slightly enhanced star formation, and SFR is comparable to that in the disc of NGC 4567.

Figures 5(b) and 6(b) show the distributions of SFE_{mol} and SFE_{gas} in VV 219. The spiral arms in NGC 4567 show higher SFEs. In particular, the southwestern arm has the highest SFEs. Another region with high SFEs is seen near the centre of NGC 4568, as often seen in spiral galaxies. The overlap region also shows a slight enhancement of SFEs, although it is insignificant when considering the uncertainty. However, high angular resolution CO image ($2'' \times 2''$) shows H α blobs are found where CO emission is weak (figure 3 in Kaneko et al. 2018). Therefore, SFEs are actually enhanced in the overlap region.

Figures 4(c), 5(c), and 6(c) are the maps of SFR, SFE_{mol} and SFE_{gas} of VV 254, respectively. The VV 254 system also shows relatively simple distributions of SFR and SFEs like the VV 219 system. High star formation activities are seen in the centre of UGC 12914 (bottom-right) and UGC 12915 (top-left), although UGC 12915 is a more active star-forming galaxy. Additionally, a region showing high SFR in UGC 12915 is slightly extended toward the overlap region, corresponding to the star-forming region previously reported by Komugi et al. (2012). Star formation in UGC 12914 is associated with the warped stellar disc. Star formation is not active in the overlap region despite a large amount of molecular gas and atomic gas.

Unlike SFR, the highest SFE_{mol} and SFE_{gas} locate at $< 10''$ to the south from the centre of UGC 12915. This region also does not correspond to the peak of CO. Higher angular-resolution CO data obtained by Iono, Yun & Ho (2005) shows a giant molecular cloud apart from the disc of UGC 12915. The position of this cloud matches the location of the highest SFE_{mol} and SFE_{gas} of VV 254. Therefore, the high SFE_{mol} and SFE_{gas} may be due to the active star formation of this cloud. In UGC 12914, SFE_{mol} and SFE_{gas} in the warped part of the disc (the northern disc) are higher than in a non-warped part. However, due to the low CO sensitivity, we cannot see the distributions of SFEs in the outer disc of UGC 12914 in this study.

The Antennae Galaxies

Figures 4(d), 5(d), and 6(d) reveal that star-forming regions are embedded along the stellar tidal arms of the Antennae Galaxies. A peak of SFR in NGC 4038 (top) is at its centre, while a peak of NGC 4039 (bottom) is off the centre. Besides, most intense star formation occurs at the southern overlap region reaching as high as $\sim 10^{-6} M_{\odot} \text{ yr}^{-1} \text{ pc}^{-2}$ where supergiant molecular complexes ($5 \times 10^5 - 9 \times 10^8 M_{\odot}$) (Wilson et al. 2000) and superstar clusters ($> 10^5 M_{\odot}$) (Whitmore et al. 1999; Zhang & Fall 1999) have been found. Although the overlap region shows higher star formation activity compared to the other regions with rich CO, the peak of SFR does not coincide with the peak of CO as other interacting galaxies.

The maps of SFEs (figure 5(d)) show that the most efficient star formation is seen at the southern overlap region, which corresponds to the peak of SFR and the SGMC 4-5 in Wilson et al. (2000), while SFE in the peak of CO in the overlap region, which is the SGMC 1, is not so high. The second most efficient star formation is seen at a branching point of the southern tidal arm of NGC 4038. The central regions of both galaxies undergo relatively calm star formation.

Even in the calm star-forming region, SFE is one order higher than other interacting galaxies. We note that figure 6(d) shows the highest SFE_{mol} at the branching point of the tidal arm of NGC 4038 and the overlap region. In this region, a strong [N II] line, suggesting massive star formation, is detected. On the other hand, CO is just above 1σ detection level in our single-dish data, and the interferometric CO image shows no CO emission (Wilson et al. 2000). These facts imply that molecular gas is few and diffuse in this region.

5.2 Causes of an enhancement of star formation efficiency

In isolated spiral galaxies, SFE is almost constant where H_2 is dominant in the ISM (the inner part of galaxies) and decreases with increasing galactic radius (Rownd & Young 1999; Leroy et al. 2008). Barred galaxies tend to show local SFE peaks at their bar-end (Muraoka et al. 2009; Maeda et al. 2020). SFE of spiral galaxies has typically symmetric distribution.

On the other hand, we found local (asymmetric and off-centre) enhancement of SFE in interacting galaxies. Although the number of targets is too small to show a unified enhancement mechanism, it would be meaningful to investigate reasons for local enhancement. Here we discuss the cause of the enhancement of SFE of our targets. The main topics are: (1) a possibility of environmental effects by a galaxy cluster rather than galaxy interaction, (2) a cause of high SFE in the secondary galaxy of a minor merger, and (3) a trigger of higher SFE at the collision front.

5.2.1 Ram pressure compression in a galaxy cluster

First, we examine the possibility of high SFE in NGC 4567, which constructs the VV 219 pair, due to the environmental effect from a cluster. VV 219 is located at a projected distance of ~ 1 Mpc from the centre of Virgo Cluster. NGC 4567 is known as an HI-deficient galaxy (Gavazzi et al. 2005). These facts imply that NGC 4567 may be suffered from ram pressure from the cluster. Ram pressure can strip HI gas in the outer disc and compress the remaining HI gas in HI-deficient galaxies. Kenney & Young (1989) compared thermal, magnetic, turbulent, and gravitational energy density with ram pressure for molecular clouds and showed that ram pressure might be one order of magnitude less than gravitational and turbulent energy densities. Since turbulent and magnetic forces balance gravity in molecular clouds in their estimate, ram pressure is not important to compress molecular clouds. Thus, we expect that enhancement on star formation activity is not caused by ram pressure based on their scenario.

On the other hand, Bekki & Couch (2003) demonstrated using hydrodynamical simulations that ram pressure compresses a self-gravitating cloud and triggers star formation

in a cloud. Some galaxies show star formation triggered by ram pressure in Virgo Cluster (Koopmann & Kenney 2004; Cramer et al. 2020). However, the fact that star-forming regions triggered by ram pressure are concentrated on the edge of the galactic disc in these galaxies implies that an influence of ram pressure is local. If the ram pressure is perpendicular to the disc of NGC 4567, gas compression should happen on the whole disc. In that case, SFE may get equally higher in the disc by ram pressure. However, it is difficult to explain high SFE in the disc of NGC 4567 only with the ram pressure since spiral arms of NGC 4567 show higher SFE. We conclude that ram pressure is not the main trigger of high SFE in the disc of NGC 4567.

5.2.2 An effect of galaxy mass ratio

Next, we investigate a reason for high SFE in the secondary galaxy. Arp 84 and VV 219 show higher SFEs are found in the secondary galaxy (i.e., NGC 5394 and NGC 4567) of the pair. Several studies have pointed out that the influence of the mass ratio of galaxies is important for star formation history during the interaction. More active star formation is reported in a secondary galaxy of minor interacting pairs (Li et al. 2008; Woods & Geller 2007). Simulations have shown that galaxy interactions transfer angular momentum from gas to stars, which moves gas to the centre of progenitors (Barnes & Hernquist 1996). Therefore, these cases can be interpreted that the primary galaxy is not tidally disturbed enough to induce radial gas infall that enhances star formation activity. In contrast, the secondary galaxy experiences a significant tidal force.

To determine if this effect predominates in the early stage, we calculate the dynamical mass ratio of the target interacting galaxies. Although the dynamical mass ratios of NGC 5395 and NGC 5394, and NGC 4568 and NGC 4567 are estimated as ~ 100 and ~ 10 , respectively, according to Iono, Yun & Ho (2005), they did not correct the inclination in deriving the dynamical mass. We re-calculate the dynamical mass considering the inclination of galaxies. The dynamical mass can be derived through the equation below:

$$M_{\text{dyn}} [M_{\odot}] = 2.32 \times 10^5 \left(\frac{R_{\text{edge}}}{\text{kpc}} \right) \left(\frac{V_{\text{corr}}}{\text{km s}^{-1}} \right)^2, \quad (11)$$

where R_{edge} is the maximum radius where emission is detected above 3σ significance level, and $V_{\text{corr}} (= V_{\text{rot}}/\sin i)$ is inclination corrected radial velocity. V_{rot} is derived by $|V_{\text{obs}}(R_{\text{edge}}) - V_{\text{sys}}|$, where $V_{\text{obs}}(R_{\text{edge}})$ is the observed velocity at R_{edge} , and V_{sys} is the systemic velocity. We calculate the dynamical mass from both CO and HI data and summarise it in table 8. Because of its nearly face-on disc of NGC 5394, a mass ratio for Arp 84 has a large uncertainty. Therefore, we adopt the mass ratio of Arp 84 from the numerical simulation by Kaufman et al. (1999).

Table 8. The dynamical mass of targets.

Galaxy	Dynamical Mass [M_{\odot}]		Mass Ratio	
	H I	CO	H I	CO
NGC 5394	$>2.4 \times 10^9$	$>9.4 \times 10^9$		
NGC 5395	4.5×10^{11}	2.8×10^{11}	<188	<30
NGC 4567	2.1×10^{10}	2.2×10^{10}		
NGC 4568	9.4×10^{10}	8.1×10^{10}	4.5	3.7
UGC 12914	6.3×10^{11}	2.7×10^{10}		
UGC 12915	2.7×10^{11}	2.7×10^{10}	2.3	1.0
The Antennae Galaxies	—	—	—	—

They assumed that NGC 5395 is 4 times heavier than NGC 5394 (i.e., the mass ratio of 4) and successfully reproduced the morphology of Arp 84. If we use this mass ratio of 4, Arp 84 is a minor merger (a mass ratio > 3). Since VV 219 has a mass ratio larger than 3 estimated from both CO and H I data, VV 219 is also a minor merger. We conclude that Arp 84 and VV 219 can be regarded as an early phase of a minor merger. Based on the unequal-mass galaxy merger simulations (mass ratio of from 2.3 to > 20) (Cox et al. 2008), star formation activity in the secondary galaxy is significantly affected by gravitational perturbation. Although it makes a small contribution to the overall SFR of the pair, the enhancement of SFR in the secondary galaxy could be larger than that in the primary galaxy. This suggests that SFE in the secondary galaxy is higher than that in the primary galaxy.

However, the distributions of star-forming regions may be different from simulations. In the simulations, star formation occurs in the gas concentrated into the central region by an interaction (e.g., Barnes & Hernquist 1996; Teyssier, Chapon & Bournaud 2010). On the other hand, star-forming regions of NGC 5394 and NGC 4567 are distributed over the whole disc ($H\alpha$ emission is seen not only in the central region of NGC 5394 but also in the edge of the northern tidal arm, which is slightly outside the field of view of CO (Roche et al. 2015)). The central concentration of molecular gas is still low compared with that of stars in these galaxies (see Paper I).

We have suggested that largely prevailed shocks throughout the disc of galaxies in Paper II. Roche et al. (2015) indicated that high $[N II]/H\alpha$ and other line ratios of the outer region of NGC 5394 are explained as a composite of shock and H II region. Similarly, other interacting galaxies also show the off-centre and widely-spread shock (e.g., Rich, Kewley & Dopita 2011; Wild et al. 2014; Saito et al. 2015). If a shock occurs during the interaction, the shock in secondary galaxies should be stronger than that in primary galaxies due to the relative strength

of a gravitational disturbance. Gas compressed by the shock leads to form stars efficiently. Hence, our finding that secondary galaxies show higher SFE spreading over the whole discs is consistent with the existence of such shocks. Other pairs in an early phase of minor tidal interaction also show active star formation in the disc of secondary galaxies, as shown in Koopmann & Kenney (2004). This fact implies that an enhancement of star formation activity in the galactic disc of a secondary galaxy seems to be a rather general phenomenon in the early phase of the minor merger. Although the disturbance of the velocity field, which indicates shocks, was not found with our resolution in the discs of NGC 4567, a shock tracer observation with higher angular resolution may reveal direct evidence of the shocks.

5.2.3 High SFE at a collision front

We consider the fact that a slight enhancement of SFEs is seen at the collision interface of Arp 84 and VV 219. This can be naturally explained by star formation triggered by the compression of the gas at the interface. High-resolution simulations by Saitoh et al. (2009) reproduced the shock-induced starburst at the interface. They showed that a giant filament of ISM is formed at the interface, and then starburst is induced there. Kaneko et al. (2018) clearly showed the large filamentary molecular collision front in the overlap region of VV 219. Although the star formation at the collision interface of Arp 84 and VV 219 is not as strong as demonstrated by Saitoh et al. (2009), there are a few large star-forming regions in the interface (Koopmann, Kenney & Young 2001; Kaufman et al. 1999). These star-forming regions have higher SFEs, as shown in figures 5(b) and 6(b). Therefore, such star-forming regions at the collision front may be at the onset phase of starburst. Supergiant molecular complexes and superstar clusters have been found in the Antennae Galaxies (Whitmore et al. 1999; Wilson et al. 2003), which are in the more advanced stage of the interaction and show higher star-forming activity than other pairs. The shock-induced star formation is the cause of the enhancement of SFE at the colliding regions.

What makes a difference in star formation activity at the overlap region among Arp 84, VV 219, and VV 254? Although these pairs possess plenty of molecular gas at their colliding region, only VV 254 does not show enhanced star formation activity there. We focus on a giant molecular cloud (GMC) collision during an interaction process. When GMC-GMC collisions happen in the overlap region, GMCs are expected to be ionised. It takes a long time, about 10^7 years, to reproduce of GMCs according to the scenario proposed by Braine et al. (2004). After the GMC reproduction, dense gas would be formed in the GMCs. Once dense gas is formed in re-formed GMCs, star formation would occur co-instantaneously. Off-course, The dense gas

formation time scale after ionisation of GMCs requires longer than the GMC reproduction time scale of 10^7 years. However, the collision age of VV 254 (2×10^7 years) is comparable to the GMC reproduction time scale. In case that a face-on collision of VV 254 ionises most GMCs in discs of progenitors, the star formation activity becomes depressed until dense molecular gas is formed in GMCs. From figures 5(c) and 6(c), we can see that star formation activity is low even existing rich molecular gas with high molecular gas fraction in the overlap region of VV 254. Although constituent galaxies of Arp 84 and VV 219 are still close, the time after the collision of these pairs might be longer than the dense gas formation time scale. If that is the case, the difference of star formation activity at the overlap region among Arp 84, VV 219, and VV 254 is attributed to the time after the collision.

Another way to explain the difference of SFE at the collision interface could be the difference in the relative velocity of two galaxies. According to the discussion about HI gas by Condon et al. (1993), the relative velocity of UGC 12914 and UGC 12915 is about 600 km s^{-1} . The relative velocities of progenitors for Arp 84 and VV 219 are only 100 km s^{-1} and 50 km s^{-1} , respectively. When the relative velocity is large, the GMCs are ionised due to the collision. Once the gas is ionised, it takes a long time to reproduce the GMC again. This effect decreases the SFE just after the collision. Thus, the collision front of interacting galaxies with high relative velocity like a prograde-prograde edge-on collision (e.g., VV 254 pair) may show active star formation with low SFE.

6 Resolved Kennicutt–Schmidt law

We examine the spatially resolved Kennicutt–Schmidt law in this section. As previously stated, we find complex distributions in SFR and SFEs, and the offset between peaks of CO and SFR. Thus, it is expected that the spatially resolved Kennicutt–Schmidt law for interacting galaxies might differ from that for isolated galaxies.

In this investigation, we consider the spatial resolution of the data. Onodera et al. (2010) showed this relationship would break with higher spatial resolution than $\sim 100 \text{ pc}$. They attribute the breakdown of the law to the difference in the evolutionary stages of individual GMCs. Bigiel et al. (2008) also examined the SFR-gas relationship with different spatial resolutions. They found that the index N , the coefficient A , and the scatter are weakly correlated with a spatial resolution from 200 pc to 1 kpc , which could be attributed to stellar feedback and cloud formation on the scale $\lesssim 300 \text{ pc}$. If the stellar feedback and cloud formation are the main reason for changing the shape of the Kennicutt–Schmidt law, it is considered that

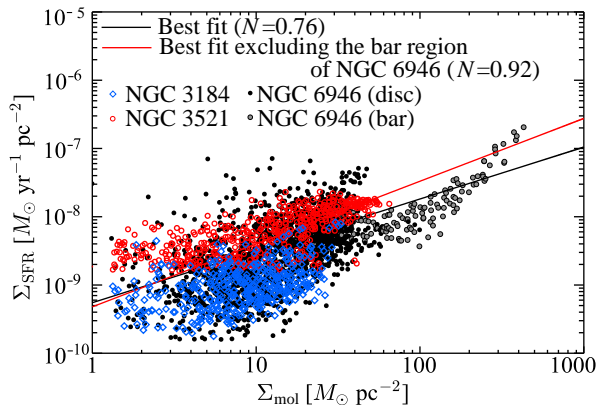


Fig. 7. Star formation rate per unit area (Σ_{SFR}) versus surface density of molecular gas (Σ_{mol}) for isolated galaxies. The black line indicates the best least-squares fit to whole data. The red line is the same as the black line but removing the data points of the bar region in NGC 6946.

index, the coefficient and the scatter are not affected on scales larger than 1 kpc. Therefore, we convolve the data to the spatial resolution of 1 kpc for the isolated spiral galaxies since the original spatial resolutions of these data for the isolated spiral galaxies are 400–700 pc. Since the spatial resolution of interacting galaxies is larger than 1 kpc, we do not convolve the resolution of these data. For this operation, the index and the coefficient can be compared between the interacting galaxies and the isolated galaxies. Note that the scatter of the interacting galaxies may be smaller than that in the isolated galaxies due to the larger spatial resolution.

For the analysis, we only use the data where CO emissions are detected higher than 3σ noise level after convolving the data for the investigation.

6.1 Tracers of the surface density of ISM

It has been discussed which value should be used as Σ_{ISM} in equation 1, namely, the surface density of total gas or molecular gas (Bigiel et al. 2008; Wong & Blitz 2002). This problem concerns an important issue what governs the physical process of conversion from interstellar gas to stars. For this reason, in the beginning, we make two plots using isolated galaxy samples to check which relationship is a principle. One is the relationship between Σ_{SFR} and the surface density of molecular gas Σ_{mol} , and another is between Σ_{SFR} and the surface density of total gas Σ_{gas} . In this investigation, NGC 3184, NGC 3521 and NGC 6946 are used as isolated galaxy samples. All fitting results are summarised in tables 9 and 10.

Figure 7 represents SFR per unit area (Σ_{SFR}) versus surface density of molecular gas (Σ_{mol}) for isolated galaxies. The black line indicates the best least-squares fit to whole data with an index of 0.76 ± 0.02 . An odd branch appears around $\Sigma_{\text{mol}} > 40 M_{\odot} \text{pc}^{-2}$ of NGC 6946. NGC 6946 is a barred galaxy, and the bar region tends to have low SFE (e.g., Momose et al.

Table 9. The fitting results for resolved $\Sigma_{\text{SFR}} - \Sigma_{\text{mol}}$ relation.

Sample	Index N	Coefficient A	Coefficient of determination R^2
Isolated Galaxies	0.76 ± 0.02	-9.26 ± 0.02	0.24
Isolated Galaxies (masked bar regions)	0.92 ± 0.02	-9.24 ± 0.02	0.27
Interacting Galaxies*	1.66 ± 0.03	-10.5 ± 0.05	0.86
Interacting Galaxies (removed Antennae Galaxies)	1.09 ± 0.05	-9.75 ± 0.07	0.51
Interacting Galaxies (removed Antennae Galaxies & VV 254)	1.16 ± 0.03	-9.72 ± 0.04	0.85

*The inclination correction for data points of Antennae Galaxies is not performed.

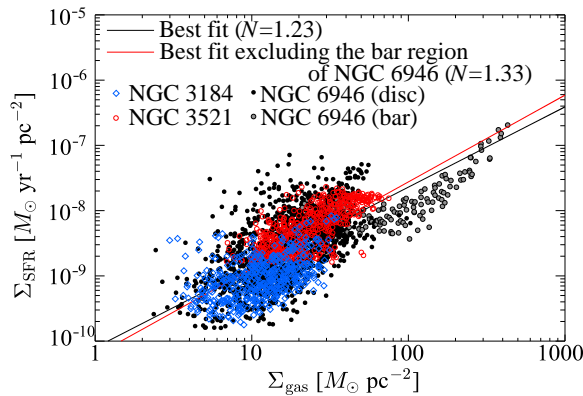
Table 10. The fitting results for resolved $\Sigma_{\text{SFR}} - \Sigma_{\text{gas}}$ relation.

Sample	Index N	Coefficient A	Coefficient of determination R^2
Isolated Galaxies	1.23 ± 0.02	-10.1 ± 0.02	0.39
Isolated Galaxies (masked bar regions)	1.33 ± 0.03	-10.2 ± 0.03	0.46
Interacting Galaxies*	1.84 ± 0.03	-10.9 ± 0.05	0.88
Interacting Galaxies (removed Antennae Galaxies)	1.28 ± 0.06	-10.2 ± 0.08	0.57
Interacting Galaxies (removed Antennae Galaxies & VV 254)	1.29 ± 0.03	-10.1 ± 0.05	0.85

*The inclination correction for data points of Antennae Galaxies is not performed.

2010; Hirota et al. 2014; Maeda et al. 2020). We performed an elliptical fit on the bar region of NGC 6946 using an optical image. We found that most points in this branch correspond to the bar region of NGC 6946. Therefore, we fitted the data again after masking the bar region of NGC 6496. The resultant red line is an index of 0.92 ± 0.02 with R^2 of 0.27.

Then, we made the same plot for the surface density of total gas (Σ_{gas}) instead of molecular gas. The result is shown in figure 8. The best least-squares fit to whole data has an index of 1.23 ± 0.02 . Since the same branch due to the bar region of NGC 6946 is found, we mask the bar region of NGC 6496 again and find the index becomes 1.33 ± 0.03 . This index is higher than those derived using Σ_{mol} as previously reported by Bigiel et al. (2008) but is

**Fig. 8.** The same as figure 7 but for star formation rate per unit area (Σ_{SFR}) versus surface density of total gas (Σ_{gas}) for isolated galaxies.

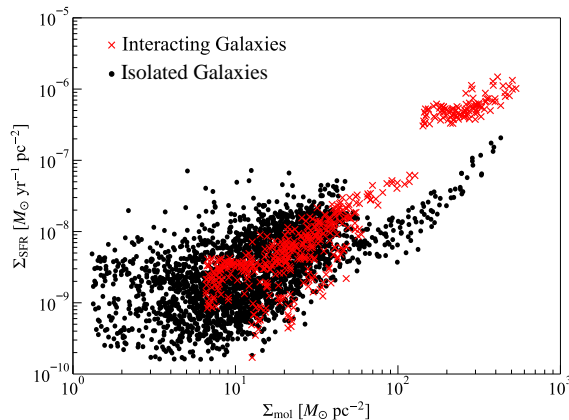


Fig. 9. A relationship of $\Sigma_{\text{SFR}}-\Sigma_{\text{mol}}$ for all interacting galaxies (red crosses) and isolated galaxies (black dots).

consistent with the value of the previous studies (Kennicutt et al. 2007). It may be due to the difference of a tracer of molecular gas. Bigiel et al. (2008) used the $\text{CO}(J = 2-1)$ line for the tracer of molecular gas, assuming a constant $\text{CO}(J = 2-1)/\text{CO}(J = 1-0)$ line ratio. However, a recent study by Yajima et al. (2021) illustrates that the $\text{CO}(J = 2-1)/\text{CO}(J = 1-0)$ line ratio differs both galaxy-to-galaxy and within a galaxy. They also point out that the index N of the Kennicutt–Schmidt law gets smaller when using a constant $\text{CO}(J = 2-1)/\text{CO}(J = 1-0)$ line ratio.

We find that the relation between Σ_{SFR} and Σ_{gas} gives a slightly better correlation ($R^2 = 0.46$) than that between Σ_{SFR} and Σ_{mol} . This result is inconsistent with Bigiel et al. (2008). They attribute it to that star formation is more directly connected with molecular gas, at least on a kpc scale, since HI gas is saturated around $\Sigma_{\text{ISM}} \simeq 10 M_{\odot} \text{pc}^{-2}$. Our result implies that HI gas also contributes to star formation, as discussed by Fukui et al. (2019).

6.2 Resolved Kennicutt–Schmidt law for interacting galaxies

Figure 9 shows a relationship between Σ_{SFR} and Σ_{mol} for interacting galaxies (red crosses) and isolated galaxies (black filled circles). In a pixel-to-pixel comparison, interacting galaxies have a similar $\Sigma_{\text{SFR}}-\Sigma_{\text{mol}}$ relation to the isolated galaxies.

We also plot each progenitor of our interacting galaxies with different symbols to see the contribution to the relation (figure 10). Even for interacting galaxies, there still exists a power-law relation with an index of 1.66 ± 0.03 .

We can see all points belonging to the Antennae Galaxies lie in the top-right region in the $\Sigma_{\text{SFR}}-\Sigma_{\text{mol}}$ plane. However, due to their severely disturbed morphology, we do not correct the inclination effect on Σ_{SFR} and Σ_{mol} for the Antennae Galaxies. The inclination correction is important about the Kennicutt–Schmidt law since the inclination correction reduces both

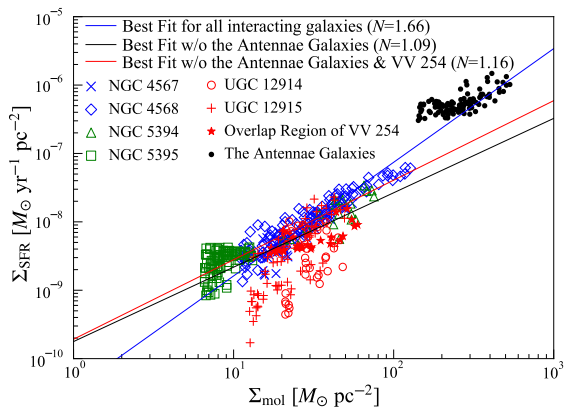


Fig. 10. A relationship of $\Sigma_{\text{SFR}}-\Sigma_{\text{mol}}$ compiling all interacting galaxies. The blue line represents the best least-squares fit to whole interacting galaxies. The black line indicates the best least-squares fit to whole interacting galaxies except for the Antennae Galaxies. The red line is the same as the black line but out of the Antennae galaxies and VV 254.

Σ_{SFR} and Σ_{mol} . Therefore, we remove the data of the Antennae Galaxies. The index of the relation becomes 1.09 ± 0.05 . This investigation corresponds to the Kennicutt-Schmidt law for only interacting galaxies in the early stage.

Suppose the inclination correction can be done on the Antennae Galaxies. In that case, the index must become larger because the inclination-corrected data from the Antennae Galaxies move to the bottom left along with the index of 1, which is higher than the result of the original fit ($N = 1.09 \pm 0.05$).

In figure 10, VV 254 (red points) show slightly different properties from other galaxies. Most data points of VV 254 exist below the fitted line of isolated spiral galaxies (Some regions have one order of magnitude lower SFR than the best-fitted line for the isolated galaxies). If we remove the data of the Antennae Galaxies and VV 254 from the power-law fitting, we find the tight relation ($R^2 = 0.85$):

$$\log \Sigma_{\text{SFR}} = -(9.72 \pm 0.04) + (1.16 \pm 0.03) \log \Sigma_{\text{mol}}. \quad (12)$$

This is consistent with the isolated spiral galaxies in both index and coefficient, as clearly seen in figure 9. Interacting galaxies in the early stage obey the relation found in the isolated spiral galaxies.

Next, we look into a relationship between Σ_{SFR} and Σ_{gas} for our sample of interacting galaxies in the early and the mid stage. Figure 11 illustrates a power-law relation, which is seen as the case of Σ_{SFR} and Σ_{mol} . By using all pixels, interacting galaxies shows a power-law relation with an index of 1.84 ± 0.03 .

Figure 12 represents the relationship between Σ_{SFR} and Σ_{gas} for interacting galaxies. The power-law relation still holds in the case of $\Sigma_{\text{SFR}}-\Sigma_{\text{gas}}$.

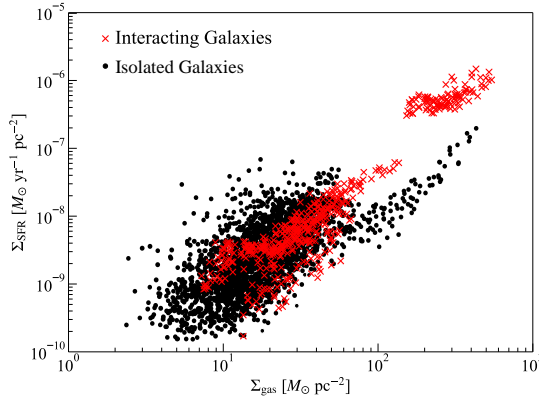


Fig. 11. The same as figure 9 but the relationship between Σ_{SFR} and Σ_{gas} .

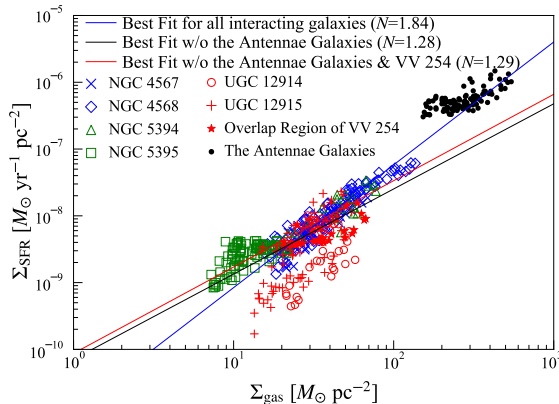


Fig. 12. The same as figure 10 but the relationship between Σ_{SFR} and Σ_{gas} .

As the inclination correction is not performed on Σ_{SFR} and Σ_{gas} for the Antennae Galaxies, we remove the data points of the Antennae Galaxies and fit again. The interacting galaxies in the early stage of interaction have a power-law index of 1.28 ± 0.06 with $R^2 = 0.57$.

VV 254 have a large scatter, and some points in VV 254 shows lower SFR (about 1 dex, which is significantly larger than the uncertainty) in $\Sigma_{\text{SFR}}-\Sigma_{\text{mol}}$ relation compared to the isolated galaxies (also see figure 11). VV 254 has the largest spatial resolution among the sample (5.8 kpc). As stated previously, a larger resolution makes a smaller scatter. Therefore, a large scatter of VV 254 cannot be explained by the difference of the angular resolution. This suggests that some physical factors cause a lower SFR in VV 254.

Then, we exclude data points of VV 254 in addition to that of the Antennae Galaxies. This results in a tight power-law relation ($R^2 = 0.85$):

$$\log \Sigma_{\text{SFR}} = -(10.06 \pm 0.05) + (1.29 \pm 0.03) \log \Sigma_{\text{gas}}. \quad (13)$$

The Kennicutt–Schmidt law is an “averaged” relationship between Σ_{SFR} and Σ_{ISM} over the

focused region. Therefore, the law is valid only when stars are formed constantly within the region. In other words, the law becomes broken in a region where star formation activity is drastically changing in a short time (within a time scale that a used star-formation indicator traces). The Antennae Galaxies and VV 254 are good examples of this phenomenon.

To summarise our investigations about the Kennicutt–Schmidt relation, we found a tight correlation with Σ_{SFR} , whichever we use Σ_{mol} or Σ_{gas} . These Kennicutt–Schmidt laws are well consistent with isolated galaxies in the index and the coefficient, and they have super-linear indices ($N > 1$). These facts imply that the Kennicutt–Schmidt law for the interacting galaxies in the early stage is not qualitatively changed compared with the isolated galaxies. At least, the effect on star formation at the early stages of interaction is weaker than that of the bar structure. However, we also note that the Antennae Galaxies, interacting galaxies in the mid stage, maybe in enhanced star-forming phase, and VV 254, which is just after the high-velocity head-on collision, shows decreased star formation.

6.3 Star formation history in interacting galaxies

In this subsection, we discuss how the interaction affects ISM and star-forming activity based on the results of Paper II and this paper. The main key findings are the high molecular gas fraction and local enhancement of SFEs in interacting galaxies even in the early stage, but no change of the index and the coefficients in the Kennicutt–Schmidt law.

When the galaxies start colliding, ISM environments are changed first. During a collision of two galaxies, GMCs and HI clouds collide with each other and are then ionised, as discussed in Paper II. Then, ionised gas with high pressure prevails over the discs and the overlap region along with the progress of the collision. Radiative cooling makes ionised gas back into neutral hydrogen gas in a short time (Harwit et al. 1987). Such dense atomic hydrogen gas is converted into molecular hydrogen gas. The conversion time scale depends on surrounding shocked gas pressure, determined by the initial collisional parameters. As a result, the molecular gas fraction becomes higher during the collision because of the efficient transition from HI to H₂ gas.

However, at least in the early stages, there is no difference in the quality of star formation activity between interacting galaxies and isolated galaxies. From the galaxy-scale Kennicutt–Schmidt law for the interacting galaxies and the isolated galaxies, the increase in SFR is found to be within a factor of three. Similarly, there is no difference in SFE on the galaxy scale. The spatially-resolved Kennicutt–Schmidt law for interacting galaxies, which includes the data from severely disturbed galaxy NGC 5395, has a tight correlation. Its index and coefficient are

the same as that for the isolated galaxies.

Star formation occurs from a diffuse molecular cloud via high-density molecular gas. Observations of denser molecular gas tracers such as HCN and $^{12}\text{CO}(J = 3-2)$ revealed that SFE has a linear relation with a dense molecular gas fraction from giant molecular cloud to ULIRGs (Gao & Solomon 2004; Michiyama et al. 2016; Shimajiri et al. 2017). Also, recent works of Our Galaxy showed that star formation activity has a better correlation with dense gas fraction than the amount of molecular gas (Torii et al. 2019). Therefore, even if many GMCs are formed through the conversion from HI to H₂ in interacting galaxies efficiently, star formation will not occur if there is not enough dense gas inside them. Thus, high SFEs are achieved only when dense gas is efficiently produced on the target scale. VV254 is low SFR and SFEs, although it has a large amount of molecular gas, which can be traced by CO. The gas ionised by the collision returns to GMCs within a short time and becomes a large amount of molecular gas, but it is thought that it has not yet produced dense gas. Low SFR and SFE in VV 254 imply that VV 254 are just ongoing the formation process of GMCs from ionised gas and not enough time for star formation yet. When the time elapsed enough after the first collision, dense molecular gas could be formed at the colliding area (it could be the overlap region). Local active star formation with high SFE occurs in that region, although the SFR and SFE in a galaxy scale are still low.

On the other hand, the situation changes in the later stage of interaction. As suggested from Paper II in the Antennae Galaxies, which are the most progressed interacting galaxies among our sample, the molecular gas fraction will get much higher throughout the pair. At that phase, we may also expect that molecular gas becomes denser due to high gas concentration toward the centre (e.g., Scoville et al. 1991). Dense gas in the galaxy centre leads to start starburst such as ULIRGs. The galaxy-wide starburst would make galaxy-scale SFR and SFE high.

7 Summary

We investigated the relationship between ISM and star formation activity in interacting galaxies in the early and mid stages of the interaction using CO, HI, and dust-corrected star formation rate images. Our findings are:

1. On a galactic scale, interacting galaxies have a similar sSFR compared with the isolated sample.

2. The galactic-scale Kennicutt–Schmidt law reveals that most of our samples do not show enhanced SFR.
3. Galaxy-scale sSFR and SFE of the interacting galaxies are comparable to those of the isolated spiral galaxies.
4. SFE maps show asymmetric distributions or local peaks at off-centre regions.
5. Higher SFE in smaller progenitors could be due to largely-prevalled shock.
6. Difference of SFE at the collision front can be explained by the time after the collision and strength of shock depending on collision parameters.
7. No difference of the index and coefficient in kpc-scale Kennicutt–Schmidt law in the early stage is found between interacting galaxies in the early stage and isolated galaxies, although interacting galaxies have higher molecular gas fraction than isolated galaxies.

Funding

This work was supported by Japan Society for the Promotion of Science KAKENHI (Grant No. 18K13593).

Acknowledgement

We would like to thank all staff members of NRO for observational support. This research made use of the NASA/IPAC Extragalactic Database (NED), which is operated by the Jet Propulsion Laboratory, California Institute of Technology, under contract with the National Aeronautics and Space Administration.

Appendix. Effect of Oversampling on the Kennicutt–Schmidt law

Oversampling may affect the results of analyses. We check the robustness of our results by using two dummy maps that reproduce the index, coefficient, and scatter of the observed Kennicutt–Schmidt law. In this analysis, the first map, “map α ”, mimics the surface density of ISM (Σ_{gas}), while the second map, “map β ”, imitates the surface density of SFR (Σ_{SFR}). The two-dimensional dummy maps are made as the following steps.

1. An original source map is made to have a size of 21×21 pixels. We embed “sources”, which have Σ_{α} , a value of the map α , at i -th column and j -th row

$$\Sigma_{\alpha}(i, j) = \begin{cases} 10^{1.3-0.2[\text{abs}(11-i)]} \times 10^{1.3-0.2[\text{abs}(11-j)]} & (6 \leq i \leq 16, 6 \leq j \leq 16) \\ 0 & (\text{otherwise}) \end{cases} . \quad (\text{A1})$$

These values are set to have the similar dynamic range of the observed Σ_{gas} ($1.0 \lesssim \log \Sigma_{\text{gas}} \lesssim 2.5$).

2. The map β is made to obey a power-law relation as follows:

$$\log \Sigma_{\beta} = -10.0 + 1.3 \log \Sigma_{\alpha} \quad (\text{A2})$$

3. We add Gaussian-like noises onto “source” maps to represent thermal noise. Noises are set to have as same as the observed Σ_{gas} and Σ_{SFR} .

4. The map α and β are convolved with a Gaussian, which has FWHM of 1 pixel, to represent observations with a Gaussian-shaped beam.

5. In order to replicate data reduction due to On-The-Fly technique, the map α is convolved with a Bessel–Gaussian kernel. The Bessel-Gaussian kernel has implemented to have

$$f(r) = \begin{cases} \frac{J_1(\pi r/a)}{\pi r/a} \exp\left[-\left(\frac{r}{b}\right)^2\right] & (r \leq R_{\text{max}}) \\ 0 & (r > R_{\text{max}}). \end{cases} \quad (\text{A3})$$

where J_1 is a first-order Bessel function, r is the distance between the data point in the unit of the grid spacing. The parameters a , b , and R_{max} are set as $a = 1.55$, $b = 2.52$, and $R_{\text{max}} = 3$, which are as same as the parameters adopted in the data reduction of the CO data. With these parameters, the convolution yields an effective beam, which has 1.29 times larger beam size than the beam made in the step 4.

We make a hundred sets of these maps and derive the correlation coefficient R^2 between the map α and map β with a Nyquist rate (a sampling rate of every 2 pixels) and oversampling (a sampling rate of every 2.58 pixels). We mask the emission lower than 3σ for deriving R^2 . One of Σ_{α} - Σ_{β} plots with the Nyquist sampling and oversampling is shown in figure 13. The plot illustrates the dummy maps successfully reproduce the observed Kennicutt–Schmidt law. Although R^2 is not a ratio scale but an ordinal scale, checking R^2 distributions is effective to see the effect of difference of sampling. We derived $\Delta R^2 \equiv R^2_{\text{oversampling}} - R^2_{\text{Nyquist}}$, where $R^2_{\text{oversampling}}$ is R^2 for the oversampling case and R^2_{Nyquist} is R^2 for the Nyquist sampling case. As shown in figure 14, the dummy maps correlate with $R^2 \sim 0.8$, and ΔR^2 show an average of 0.02 in those cases. We also investigate the effect of the difference of sampling rates for indices and coefficients. Figure 15 shows that the indices and coefficients are not changed for difference of samplings. These findings mean if we sample a map with oversampling, the fitting result is slightly better than the case that the data is sampled with the Nyquist sampling in most cases (~ 90 cases). However, the sampling effect does not change the significance of the result. Therefore, our findings about the Kennicutt–Schmidt law should be real.

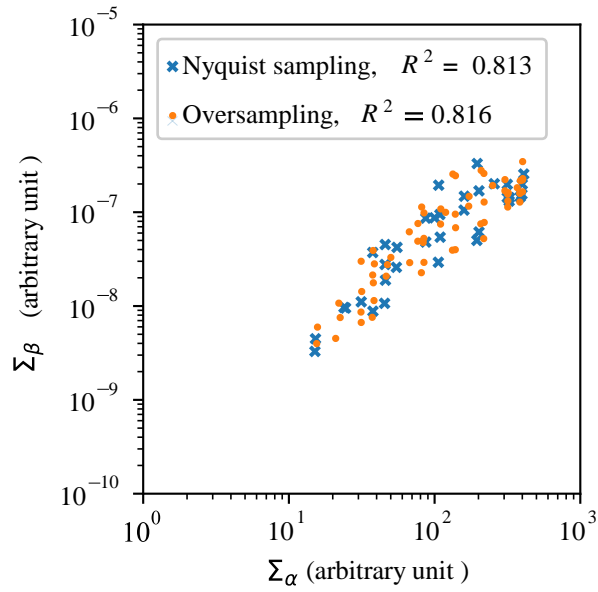


Fig. 13. An example of relationship between Σ_α and Σ_β with the Nyquist sampling and oversampling.

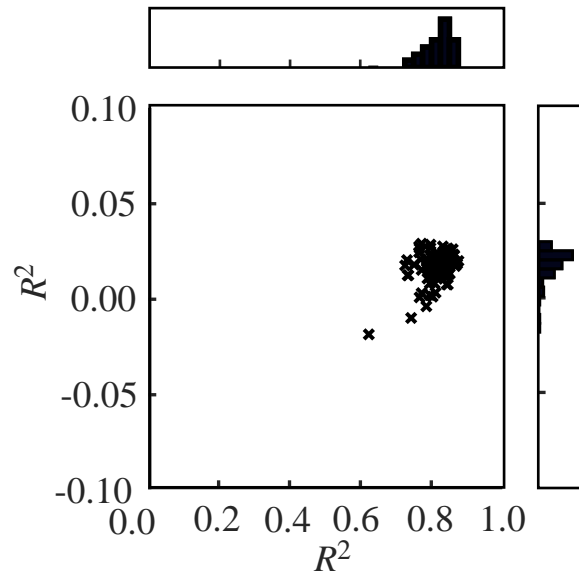


Fig. 14. Scatter plot of $R^2 - \Delta R^2$ and their histograms.

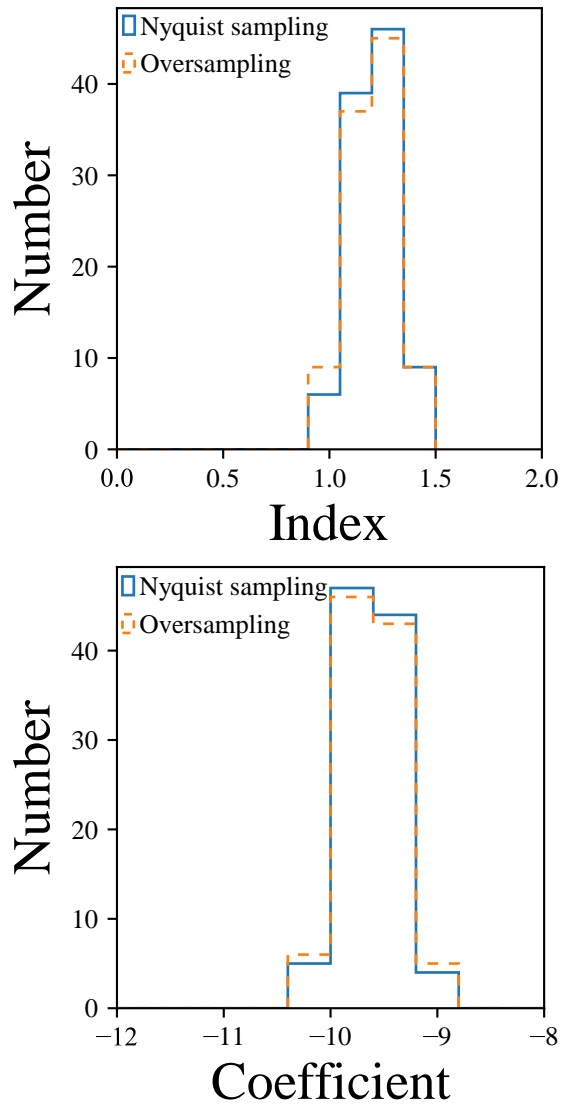


Fig. 15. Histograms of index and coefficient of the fits for mock images.

References

- Barnes, J. E. & Hernquist, L. 1996, *ApJ*, 471, 115
- Bekki, K., & Couch, W. J. 2003 *ApJL*, 596, L13
- Bell, E. F., McIntosh, D. H., Katz, N., & Weinberg, M. D. 2003 *ApJS*, 149, 289
- Bigiel, F., Leroy, A., Walter, F., Brinks, E., de Blok, W. J. G., Madore, B., & Thornley, M. D. 2008 *AJ*, 136, 2846
- Boomsma, R., Oosterloo, T. A., Fraternali, F., van der Hulst, J. M., & Sancisi, R. 2005 *A&A*, 431, 65
- Bolatto, A. D., Wolfire, M. & Leroy, A. K. 2013 *ARA&A*, 51, 207
- Braine, J., Lisenfeld, U., Duc, P.-A., Brinks, E., Charmandaris, V., & Leon, S. 2004 *A&A*, 418, 419
- Bridge, C. R., Carlberg, R. G., & Sullivan, M. 2010 *ApJ*, 709, 1067

Bruzual, G., & Charlot, S. 2003 MNRAS, 344, 1000

Bushouse, H. A. 1987 ApJ, 320, 49

Bushouse, H. A., Lamb, S. A., & Werner, M. W. 1988 ApJ, 335, 74

Calzetti, D., et al. 2007 ApJ, 666, 870

Casasola, V., Bettoni, D., & Galletta, G. 2004 A&A, 422, 941

Condon, J. J., Helou, G., Sanders, D. B., & Soifer, B. T. 1993 AJ, 105, 1730

Cox, T. J., Jonsson, P., Somerville, R. S., Primack, J. R. & Dekel, A. 2008 MNRAS, 384, 386

Cramer, W. J., et al. 2020 ApJ, 901, 95

Daddi, E., et al. 2010 ApJL, 714, L118

Dale, D. A., et al. 2005 ApJ, 633, 857

Dale, D. A., et al. 2009 ApJ, 703, 517

Dame, T. M., Hartmann, D., & Thaddeus, P. 2001 ApJ, 547, 792

Di Matteo, P., Combes, F., Melchior, A.-L. & Semelin, B. 2007 A&A, 468, 61

Fazio, G. G. et al. 2004 ApJS, 154, 10

Fukui, Y. et al. 2019 ApJ, 886, 14

Gao, Y. & Solomon, P. M. 2004 ApJ, 606, 271

Gavazzi, G., Boselli, A., van Driel, W., & O'Neil, K. 2005 A&A, 429, 439

Genzel, R., et al. 2010 MNRAS, 407, 2091

Gil de Paz, A. et al. 2007 ApJS, 173, 185

Giovanelli, R., Haynes, M. P., Myers, S. T., & Roth, J. 1986 AJ, 92, 250

Harwit, M., Houck, J. R., Soifer, B. T., & Palumbo, G. G. C. 1987 ApJ, 315, 28

Hibbard, J. E., van der Hulst, J. M., Barnes, J. E., & Rich, R. M. 2001 AJ, 122, 2969

Hirota, A., et al. 2014 PASJ, 66, 46

Hopkins, P. F., Kereš, D., Murray, N., Hernquist, L., Narayanan, D., & Hayward, C. C. 2013 MNRAS, 433, 78

Iono, D., Yun, M. S., & Mihos, J. C. 2004 ApJ, 616, 199

Iono, D., Yun, M. S., & Ho, P. T. P. 2005 ApJS, 158, 1

Jarrett, T. H., Chester, T., Cutri, R., Schneider, S. E., & Huchra, J. P. 2003 AJ, 125, 525

Kaneko, H., Kuno, N., Iono, D., Tamura, Y., Tosaki, T., Nakanishi, K., & Sawada, T. 2013 PASJ, 65, 20

Kaneko, H., Kuno, N., Iono, D., Tamura, Y., Tosaki, T., Nakanishi, K., & Sawada, T. 2017 PASJ, 69, 66

Kaneko, H., Kuno, N., & Saitoh, T. R. 2018 ApJL, 860, L14

Kaufman, M., et al. 1999 ApJ, 118, 1577

Kennicutt, Jr., R. C. et al. 2007 ApJ, 671, 333
Kennicutt, R. C. 1998 ApJ, 498, 541
Kennicutt, R. C. 1998 ARA&A, 36, 189
Kennicutt, R. C., Lee, J. C., Funes, J. G., J., S., Sakai, S., & Akiyama, S. 2008 ApJS, 178, 247
Kenney, J. D. P., & Young, J. S. 1989 ApJ, 344, 171
Knapen, J. H., Cisternas, M. & Querejeta, M. 2015 MNRAS, 454, 1742
Komugi, S., et al. 2012 ApJ, 757, 138
Koopmann, R. A., & Kenney, J. D. P. 2004 ApJ, 613, 866
Koopmann, R. A., Kenney, J. D. P., & Young, J. 2001 ApJS, 135, 125
Kuno, N., et al. 2007 PASJ, 59, 117
Leroy, A., Walter, F., Brinks, E., Bigiel, F., de Blok, W. J. G., Madore, B., & Thornley, M. D. 2008
AJ, 136, 2782
Li, C., Kauffmann, G., Heckman, T. M., Jing, Y. P. & White, S. D. M. 2008 MNRAS, 385, 1903
Liu, D., Gao, Y., Isaak, K., Daddi, E., Yang, C., Lu, N., & van der Werf, P. 2015 ApJL, 810, L14
Maeda, F., Ohta, K., Fujimoto, Y., Habe A., & Ushio, K. 2020 MNRAS, 495, 3840
Michiyama, T., et al. 2016 PASJ, 68, 96
Momose, R., Okumura, S. K., Koda, J. & Sawada, T. 2010 ApJ, 721, 383
Muraoka, K., et al. 2009 PASJ, 61, 163
Narayanan D., Krumholz M. R., Ostriker E. C., Hernquist L., 2012 MNRAS, 421, 3127
Onodera, S., et al. 2010 ApJL, 722, L127
Pan, H., et al. 2018 ApJ, 868, 132
Rich J. A., Kewley L. J., & Dopita M. A. 2011 ApJ, 734, 87
Rieke, G. H. et al. 2004 ApJS, 154, 25
Roche, N., Humphrey, A., Gomes, J. M., Papaderos, P., Lagos, P., & Sánchez, S. F. 2015 MNRAS,
453, 2349
Rownd, B. K., & Young, J. S. 1999, ApJ, 118, 670
Saintonge, A., et al. 2011 MNRAS, 415, 61
Saintonge, A., et al. 2012 ApJ, 758, 73
Saito, T., et al. 2015 ApJ, 803, 60
Saitoh, T. R., et al. 2009 PASJ, 61, 481
Sanders, D. B., Soifer, B. T., Elias, J. , Madore, B. F., Matthews, K., Neugebauer, G., & Scoville,
N. Z. 1988 ApJ, 325, 74
Sandstrom, K. M. et al. 2013 ApJ, 777, 5
Sawada, T., et al. 2008 PASJ, 60, 445

Scoville, N. Z., Sargent, A. I., Sanders, D. B. & Soifer, B. T. 1991 ApJL, 366, L5
Schmidt, M. 1959, ApJ, 129, 243
Shimajiri, Y., et al. 2017 A&A, 604, 74
Skrutskie, M. F., et al. 2006 AJ, 131, 1163
Smith, B. J., Struck, C., Hancock, M., Appleton, P. N., Charmandaris, V., & Reach, W. T. 2007 AJ, 133, 791
Stoche, J. T. 1978 AJ, 83, 348
Teyssier, R., Chapon, D., & Bournaud, F. 2010 ApJL, 720, L149
Torii, K., et al. 2019 PASJ, 71, S2
Violino, G., Ellison, S. L., Sargent, M., Coppin, K. E. K., Scudder, J. M., Mendel, T. J. & Saintonge, A. 2018 MNRAS, 476, 2591
Walter, F., Brinks, E., de Blok, W. J. G., Bigiel, F., Kennicutt, R. C., Thornley, M. D., & Leroy, A. 2008 AJ, 136, 2563
Werner, M. W., et al. 2004 ApJS, 154, 1
Whitmore, B. C., Zhang, Q., Leitherer, C., Fall, S. M., Schweizer, F., & Miller, B. W. 1999 AJ, 118, 1551
Wild, V., et al. 2014 A&A, 567, 132
Wilson, C. D., Scoville, N., Madden, S. C., & Charmandaris, V. 2000 ApJ, 542, 120
Wilson, C. D., Scoville, N., Madden, S. C., & Charmandaris, V. 2003 ApJ, 599, 1049
Wong, T. & Blitz, L. 2002 ApJ, 569, 157
Woods, D. F., & Geller, M. J. 2007, AJ, 134, 527
Xu, C., Gao, Y., Mazzarella, J., Lu, N., Sulentic, J. W., & Domingue, D. L. 2000 ApJ, 541, 644
Yajima, Y., et al. 2021 PASJ, 73, 257
Young, J. S., Allen, L. Kenney, J. D. P., Lesser, A. & Rownd, B. 1996 AJ, 112, 1903
Zhang, Q., & Fall, S. M. 1999 ApJL, 527, L81
Zhu, M., Seaquist, E. R., & Kuno, N. 2003 ApJ, 588, 243
Zhu, M., Gao, Y., Seaquist, E. R., & Dunne, L. 2007 ApJ, 134, 118
Zhu, Y.-N., Wu, H., Cao, C., & Li, H. N. 2008 ApJ, 686, 155